Open Research Online

The Open University's repository of research publications and other research outputs

The water cycle and regolith-atmosphere interaction at Gale crater, Mars

Journal Item

How to cite:

Steele, Liam J.; Balme, Matthew R.; Lewis, Stephen R. and Spiga, Aymeric (2017). The water cycle and regolith-atmosphere interaction at Gale crater, Mars. Icarus, 289 pp. 56–79.

For guidance on citations see FAQs.

© 2017 Elsevier Inc.

Version: Accepted Manuscript

Link(s) to article on publisher's website:
http://dx.doi.org/doi:10.1016/j.icarus.2017.02.010

Copyright and Moral Rights for the articles on this site are retained by the individual authors and/or other copyright owners. For more information on Open Research Online's data policy on reuse of materials please consult the policies page.

---

oro.open.ac.uk

Accepted Manuscript

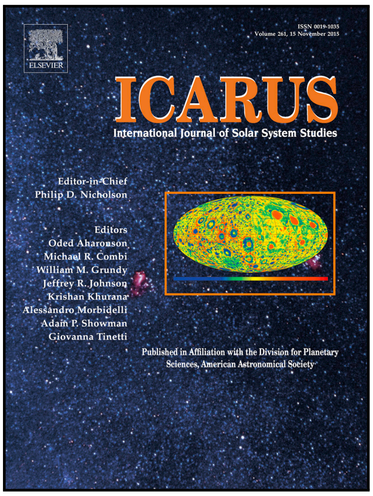

The water cycle and regolith-atmosphere interaction at Gale crater, Mars

Liam J. Steele, Matthew R. Balme, Stephen R. Lewis, Aymeric Spiga

PII: S0019-1035(16)30484-5
DOI: 10.1016/j.icarus.2017.02.010
Reference: YICAR 12369

To appear in: *Icarus*

Received date: 12 August 2016
Revised date: 12 February 2017
Accepted date: 15 February 2017

Please cite this article as: Liam J. Steele, Matthew R. Balme, Stephen R. Lewis, Aymeric Spiga, The water cycle and regolith-atmosphere interaction at Gale crater, Mars, *Icarus* (2017), doi: 10.1016/j.icarus.2017.02.010

This is a PDF file of an unedited manuscript that has been accepted for publication. As a service to our customers we are providing this early version of the manuscript. The manuscript will undergo copyediting, typesetting, and review of the resulting proof before it is published in its final form. Please note that during the production process errors may be discovered which could affect the content, and all legal disclaimers that apply to the journal pertain.

ACCEPTED MANUSCRIPT

Highlights

- We perform mesoscale simulations of the water cycle in a region around Gale crater
- Regolith interaction reduces vapour abundances at crater floor by factors of 2-3
- Nighttime subsurface ice amounts are small in all seasons
- Diffused vapour is transported up into the atmosphere at convergence boundaries
- Results at Gale crater are representative of other craters in the mesoscale domain

ACCEPTED MANUSCRIPT

ACCEPTED MANUSCRIPT

The water cycle and regolith-atmosphere interaction at Gale crater, Mars

Liam J. Steele[a,1,*], Matthew R. Balme[a], Stephen R. Lewis[a], Aymeric Spiga[b]

[a] *Department of Physical Sciences, The Open University, Walton Hall, Milton Keynes MK7 6AA, UK*
[b] *Laboratoire de Météorologie Dynamique, UMR CNRS 8539, Institut Pierre-Simon Laplace, Sorbonne Universités, UPMC Univ Paris 06, 4 place Jussieu, 75005 Paris, France*

Abstract

We perform mesoscale simulations of the water cycle in a region around Gale crater, including the diffusion of water vapour in and out of the regolith, and compare our results with measurements from the REMS instrument on board the Curiosity rover. Simulations are performed at three times of year, and show that diffusion in and out of the regolith and adsorption/desorption needs to be taken into account in order to match the diurnal variation of relative humidity measured by REMS. During the evening and night, local downslope flows transport water vapour down the walls of Gale crater. When including regolith-atmosphere interaction, the amount of vapour reaching the crater floor is reduced (by factors of 2–3 depending on season) due to vapour diffusing into the regolith along the crater walls. The transport of vapour into Gale crater is also affected by the regional katabatic flow over the dichotomy boundary, with the largest flux of vapour into the regolith initially occurring on the northern crater wall, and moving to the southern wall by early morning. Upslope winds during the day transport vapour desorbing and mixing out of the regolith up crater walls, where it can then be transported a few hundred metres into the atmosphere at convergence boundaries. Regolith-atmosphere interaction limits the formation of surface ice by reducing water vapour abundances in the lower atmosphere, though in some seasons ice can still form in the early morning on eastern crater walls. Subsurface ice amounts are small in all seasons, with ice only existing in the upper few millimetres of regolith during the night. The results at Gale crater are representative of the behaviour at other craters in the mesoscale domain.

Keywords: Mars, Mars, atmosphere, Mars, climate, Mars, surface

---

1. Introduction

Spacecraft observations, beginning with those by the Mars Atmospheric Water Detector instruments aboard the Viking orbiters (Farmer et al., 1977; Jakosky and Farmer, 1982) and followed by instruments on more recent missions (e.g. Smith, 2004; Tschimmel et al.,

---

[*] Corresponding author. Now at the Department of Geophysical Sciences, University of Chicago, Chicago, Illinois, USA.

Email address: `liamsteele@uchicago.edu` (Liam J. Steele)

2008; Smith et al., 2009; Pankine et al., 2010; Maltagliati et al., 2011, 2013), have revealed that Mars has an active water cycle. More recently, observations by the Gamma Ray Spectrometer suite of instruments aboard Mars Odyssey (Boynton et al., 2002; Feldman et al., 2004; Maurice et al., 2011) have shown that large reservoirs of water reside in the Martian subsurface.

The regolith-atmosphere interaction of water has been studied for many decades, mainly with one-dimensional models (e.g. Smoluchowski, 1968; Fanale and Jakosky, 1982; Mellon and Jakosky, 1993, 1995; Mellon et al., 2004; Aharonson and Schorghofer, 2006; Chamberlain and Boynton, 2007), but also with global circulation models (Tokano, 2003; Böttger et al., 2004, 2005). However, these studies lack comparisons with observations to constrain the diurnal and seasonal variations in the regolith-atmosphere exchange of water. While the Imager for Mars Pathfinder was the first instrument to measure atmospheric water from the surface of Mars, by imaging the Sun in the morning and evening when it was close to the horizon (Titov et al., 1999), the thermal and electrical conductivity probe (TECP) on the Phoenix lander was the first to take in-situ measurements using a relative humidity sensor (Zent et al., 2010; Rivera-Valentin and Chevrier, 2015; Zent et al., 2016). Revised results from the Phoenix TECP show that water vapour diffuses into the regolith mainly in the late afternoon, and that early mornings are the most humid part of the day due to the sublimation of surface ice formed at night (Zent et al., 2016). However, the Pathfinder and Phoenix landers were only operational for 85 and 152 sols respectively, and were not equipped with the necessary instrumentation to perform detailed studies of the near-surface water distribution. Additionally, the topography of Gale crater is likely to result in a more complex water cycle than that experienced by Phoenix in the northern plains.

The Curiosity rover landed on the floor of Gale crater in late northern hemisphere summer ($L_\mathrm{S} = 151°$) of Mars Year (MY) 31. Since $L_\mathrm{S} = 154°$, the Rover Environmental Monitoring Station (REMS) has been providing hourly measurements of, amongst other quantities, relative humidity, temperature and surface pressure (Gómez-Elvira et al., 2012, 2014; Harri et al., 2014a). This dataset, covering more than one Mars year, is ideal for investigating the regolith-atmosphere exchange of water. REMS observations from MSL sols 15–17 and 80–82 have recently been interpreted using a one-dimensional subsurface-atmosphere model (Savijärvi et al., 2015, 2016), while temperature and relative humidity data have been used to infer the presence of nighttime transient liquid brines (Martín-Torres et al., 2015). The seasonal variation of the circulation in and around Gale crater has been investigated in detail through mesoscale modelling studies (Tyler and Barnes, 2013, 2015; Guzewich et al., 2016; Pla-Garcia et al., 2016; Rafkin et al., 2016) and analysis of REMS pressure data (Haberle et al., 2014; Harri et al., 2014b), though these simulations have not modelled the water cycle.

In this paper we use a three-dimensional mesoscale model of the Martian atmosphere, coupled to a sub-surface regolith model, and focus on the regolith-atmosphere interaction of water, as well as the effects of the atmospheric circulation on the water distribution. The

ACCEPTED MANUSCRIPT

ACCEPTED MANUSCRIPT

goal of the paper is not to provide the best possible match to individual REMS measurements, through constant refining of surface and atmospheric properties. It is to understand the interaction between the surface and atmosphere on a regional scale, with the REMS measurements acting as a way of validating the regolith model results.

2. Model description and simulations performed

2.1. Mesoscale model

The mesoscale model we use was developed at the Laboratoire de Météorologie Dynamique (Spiga and Forget, 2009). It is based on the Weather Research and Forecasting dynamical core (Skamarock and Klemp, 2008), and uses the same physical parameterizations (radiative transfer, turbulent mixing, cloud formation) as the ones developed for global circulation model (GCM) studies (e.g. Forget et al., 1999; Spiga and Forget, 2009).

As Gale crater lies on the dichotomy boundary, it is affected by large-scale slope flows associated with this dichotomy (e.g. Tyler and Barnes, 2013; Rafkin et al., 2016). In order to capture these flows, we use a nested grid configuration, with a parent domain (domain 1) and two nested domains (domains 2 and 3); see Figure 1. Each domain has 146×146 grid points in latitude and longitude. At the location of Gale crater, the resolution is 54 km for the parent domain, and 18 km and 6 km for the two nests. (Due to the large areas of domains 1 and 2, the resolution varies with latitude. For example, at the southern boundary, the grid box sizes in domains 1 and 2 are 25 km and 15.5 km respectively.) There are 50 vertical levels, extending to an altitude of ~50 km. Two-way nesting is used, in which the boundary conditions for each nest come from their parent grid, and the solution from each nest replaces that on its parent grid. The time steps for domains 1–3 are 20 s, 10 s and 5 s respectively. The static surface fields (topography, thermal inertia and albedo) are derived from spacecraft data at a resolution of 64 pixels per degree, and are the same as those used by Spiga and Forget (2009).

Water vapour (referred to hereafter as simply vapour) and water ice mass mixing ratios are transported as tracers, with the microphysics scheme of Montmessin et al. (2004) used for the formation and sedimentation of ice particles (clouds are not radiatively active). If more than 5 pr-μm of water ice is deposited onto the surface, the albedo is changed to that of water ice (0.4). Dust particles are not transported, and instead we set the vertical profile of dust to follow a modified Conrath distribution (e.g. Lewis et al., 1999), with the altitude of the dust top varying with solar longitude and latitude as in Montmessin et al. (2004). Column dust opacities are obtained from daily maps produced by the binning and kriging of spacecraft data (Montabone et al., 2015). The scavenging of dust by water ice clouds is not taken into account, and any feedback between the dust and water cycles is not considered.

The regolith model is an updated version of that used by Böttger et al. (2004, 2005), which was based on the one-dimensional model of Zent et al. (1993). Full details of the

ACCEPTED MANUSCRIPT

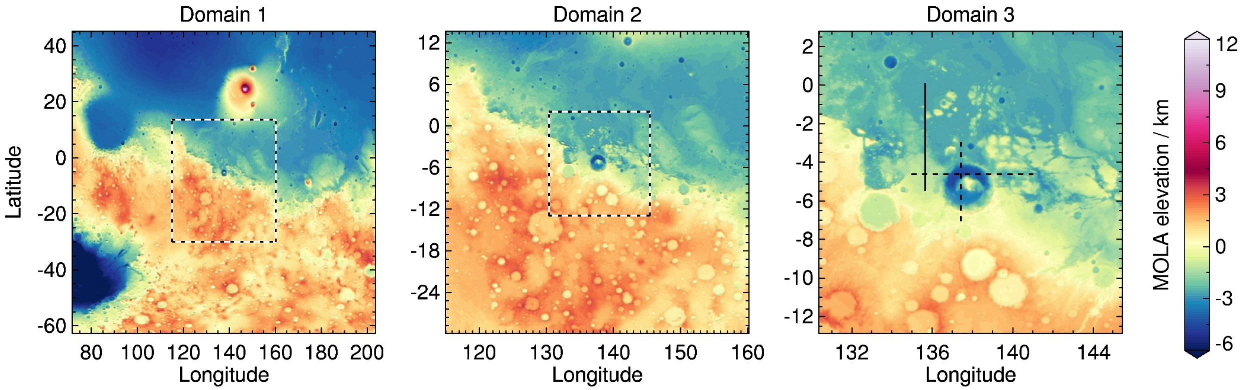

Figure 1: The three domains of the mesoscale model. Domain 3 is nested in domain 2, which is nested in domain 1 (see the boxes with black and white borders for the nest locations). The grid spacing at the location of Gale crater is 54 km, 18 km and 6 km in domains 1–3 respectively. Shading shows Mars Orbiter Laser Altimeter (MOLA) elevation data. The black dashed lines in domain 3 show the locations of the cross-sections in Figures 11, 15, 24 and 28, while the solid black line shows the location of the cross-sections in Figure 13.

scheme are given in Steele et al. (2017), so here we only give a brief overview. Diffusion of temperature and vapour, the phase changes of water, and adsorption/desorption of water vapour are calculated on 18 unevenly-spaced levels extending to ∼20 m below the surface. The concentration of water in a volume of regolith is decomposed into three states: vapour contained within the pore spaces (n), water adsorbed onto regolith grains (α) and pore ice. Both Fickian and Knudsen diffusion are accounted for, with the diffusion coefficient varying in time and space. We assume an ice-free porosity of 0.4, which was found to give a good match to REMS data in the one-dimensional simulations of Savijärvi et al. (2016), and a pore size of 10 μm. While the presence of surface CO_2 ice or water ice shuts off the regolith-atmosphere exchange, redistribution of water in the regolith can still occur (though at a much slower rate) through diffusion and phase changes.

2.2. Simulations performed

We look at three different times of year, corresponding to southern hemisphere early spring ($L_S = 187.8$–$193.1°$), late summer ($L_S = 319.8$–$325.0°$) and around aphelion ($L_S = 68.3$–$72.3°$). These periods were chosen as they encompass a range of atmospheric water contents around Gale crater, with atmospheric vapour column abundances roughly halving in each successive period. Early southern spring and aphelion are also around the times of the maximum and minimum annual vapour column abundances respectively.

Each simulation lasts for 12 sols, with the results from the first two sols ignored, allowing time for the model to ‘spin up’. For each period, we perform mesoscale simulations using three different adsorption isotherms (detailed below), as well as simulations with no regolith-atmosphere interaction. Model results are compared with REMS measurements from MY 31, 32 and 33, obtained at a height of ∼1.6 m above the ground. (The data are from the Planetary Data System atmosphere node.) We take the median of the first 10 humidity

Isotherm	$A_\mathrm{r}/10^4$ m^2 kg^{-1}	$K_0/10^{-9}$ Pa^{-1}	ϵ	ν
J97	10	15.7	2573.9	0.48
Z97	1.7	7.54	2697.2	0.4734

Table 1: Values used in the adsorption isotherms of Jakosky et al. (1997) and Zent and Quinn (1997).

measurements each hour, which are obtained when the sensor head is at roughly the same temperature as the air, and the mean of the first 10 air temperature measurements (to remove the effects of turbulence). This is the same as the procedure used by Savijärvi et al. (2015, 2016). The uncertainties in the relative humidity measurements are generally around ±2% from midday to 18:00, and ±10% at other times of day. To calculate relative humidity in the model, the Goff-Gratch equation is used to obtain the saturation vapour pressure, e_s:

$$\log_{10}(e_\mathrm{S}) = a - bT - c/T + d\log_{10} T, \tag{1}$$

with $a = 2.07023$, $b = 0.00320991$, $c = 2484.896$ and $d = 3.56654$. The relative humidity then follows via RH $= e/e_\mathrm{S}$, with e being the partial pressure of vapour (calculated from the vapour mass mixing ratio).

For the adsorption of water onto regolith grains, we consider three adsorption isotherms. The first is that from basalt powder measurements by Fanale and Cannon (1971), which we refer to hereafter as the F71 isotherm. This is given by

$$\alpha(p,T) = \rho_\mathrm{r}\beta p^{0.51}\exp(\delta/T), \tag{2}$$

where $\rho_\mathrm{r} = 1500$ kg m^{-3} is the density of the regolith, p is the partial pressure of vapour, T is the temperature, $\beta = 2.043 \times 10^{-8}$ Pa^{-1} and $\delta = 2679.8$ K. This isotherm has been used extensively in previous studies of regolith diffusion (Zent et al., 1993; Mellon and Jakosky, 1993, 1995; Mellon et al., 1997; Böttger et al., 2004, 2005). The remaining two adsorption isotherms use the Freundlich isotherm for adsorption onto palagonite, which, for the low vapour pressures encountered on Mars, can be simplified to

$$\alpha(p,T) = \rho_\mathrm{r}A_\mathrm{r}M_\mathrm{i}(pK^*)^\nu, \tag{3}$$

where A_r is the specific surface area of the regolith, $M_\mathrm{i} = 2.84 \times 10^{-7}$ kg m^{-2} is the surface mass density of a monolayer of water molecules, and $K^* = K_0\exp(\epsilon/T)$. For the isotherms of Jakosky et al. (1997) and Zent and Quinn (1997), referred to hereafter as the J97 and Z97 isotherms respectively, the specific values used in Equation 3 are given in Table 1. The J97 isotherm has been used in one-dimensional simulations by Schorghofer and Aharonson (2005) to study the stability of subsurface ice, while the Z97 isotherm has been used by Tokano (2003). Savijärvi et al. (2016) used the F71 and J97 isotherms in their one-dimensional simulations at the Curiosity rover location. Figure 2 shows how the amount

ACCEPTED MANUSCRIPT

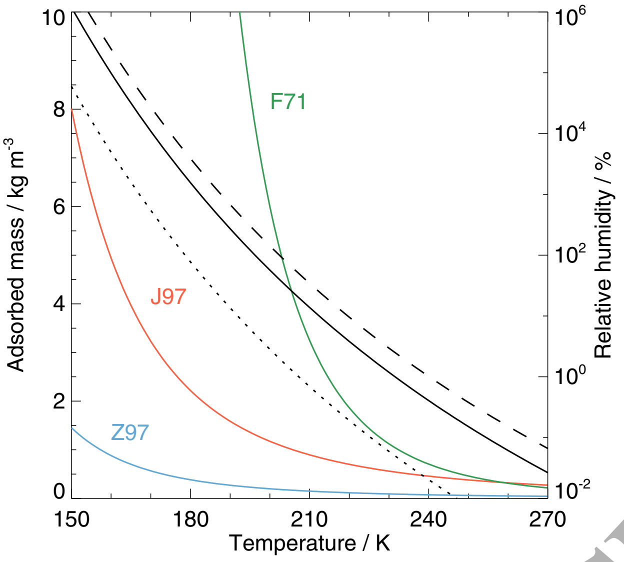

Figure 2: Amount of water adsorbed onto regolith grains for three different adsorption isotherms (coloured lines) and relative humidity (black lines) as a function of temperature. Adsorbed values assume a water vapour concentration of 10^{-6} kg m^{-3}. Relative humidities are shown for three different water vapour concentrations, corresponding to typical values (10^{-6} kg m^{-3}, solid line) as well as peak daytime (2.5×10^{-6} kg m^{-3}, dashed line) and minimum nighttime (5×10^{-8} kg m^{-3}, dotted line) values.

of water adsorbed onto the regolith grains varies with temperature for the three isotherms, assuming a vapour concentration of 10^{-6} kg m^{-3} (a typical near-surface value determined from GCM simulations, corresponding to ∼50 mg kg^{-1} or ∼100 ppmv).

2.3. Initial and boundary conditions

For comparison with the REMS measurements, we want the best possible representation of the atmospheric temperature and water distribution. As such, the initial and boundary conditions of the mesoscale model are provided by output from a GCM coupled with a data assimilation scheme. (Boundary conditions are provided at hourly intervals.) The GCM is thoroughly described elsewhere (Forget et al., 1999; Lewis et al., 1999, 2007) so we will not do so again here. Briefly, the GCM has a spectral dynamical core, an energy and angular momentum conserving vertical finite-difference scheme, a semi-Lagrangian advection scheme for tracers, and includes the physical schemes detailed in Spiga and Forget (2009). The regolith model detailed in Steele et al. (2017) is also included. The GCM was run at a resolution equivalent to 2.5° in latitude and longitude, which results in 43 and 53 GCM grid boxes spanning the east-west and north-south boundaries of the parent domain respectively.

Assimilations were performed for the three periods studied, and were run for 60 sols prior to the required dates to allow the GCMs subsurface water content to reach equilibrium. The REMS measurements considered here are for MY 31 and 32, for which Mars Climate Sounder (MCS) temperature profiles are available. These profiles extend to an altitude of ∼85 km, with a vertical resolution of ∼5 km, and comprise two sets of 12 strips of data

ACCEPTED MANUSCRIPT

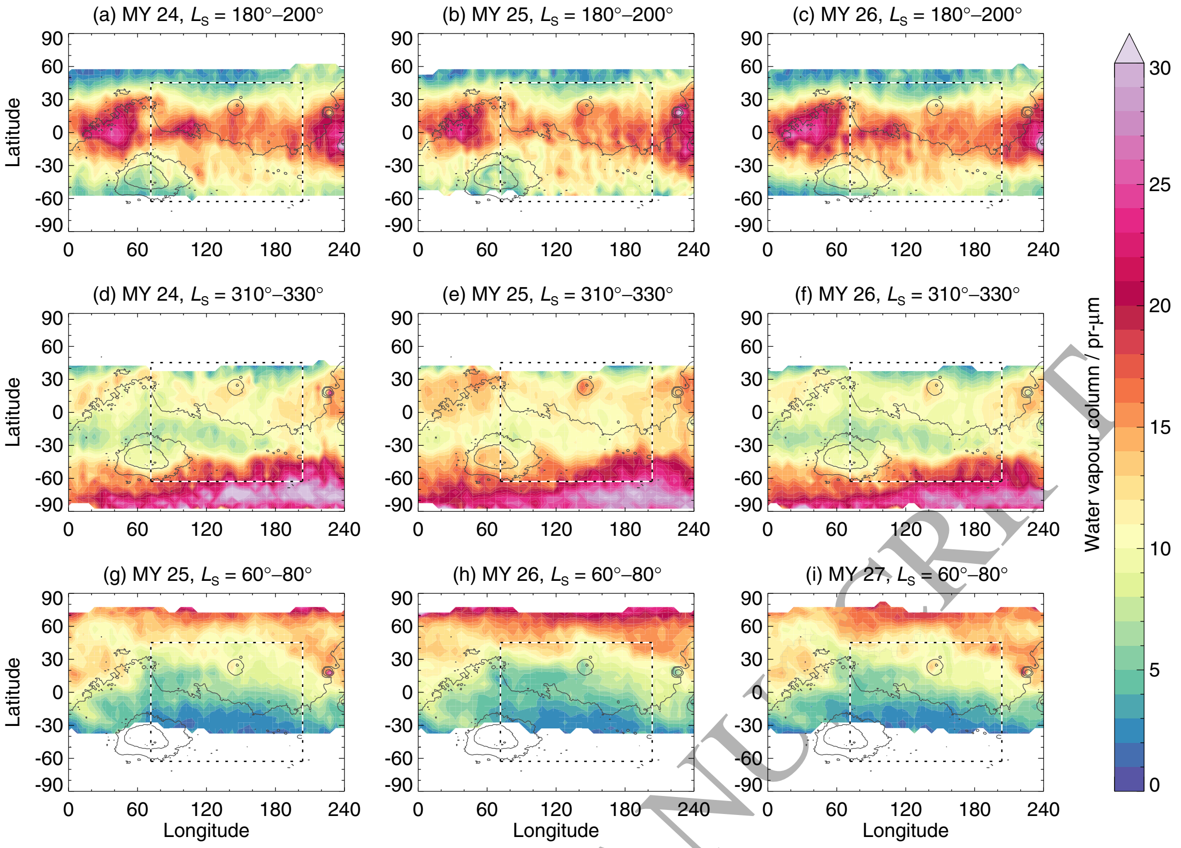

Figure 3: Water vapour column distributions in and around the parent domain (shown by the black and white rectangle) for different Mars years. Data are from TES observations (Smith, 2004), and are binned by 5° in latitude and longitude and 20° in L_S (the Mars years and L_S ranges are labelled above each plot). Black contours show topography, while white regions show where no TES data are available.

ACCEPTED MANUSCRIPT

per sol, separated by ∼30° in longitude. The data occur at local times of around 03:00 and 15:00 away from the poles (McCleese et al., 2010). MCS temperature profiles have been successfully assimilated previously (Steele et al., 2014a,b), following the procedure outlined in (Lewis et al., 2007).

For vapour, there are no data with suitable spatial and temporal coverage to assimilate for MY 31 and 32, but data are available for MY 24–27 in the form of vapour columns from the Thermal Emission Spectrometer (TES) instrument (Smith, 2004). The vapour distribution is mainly affected by the occurrence of dust storms during perihelion (Smith, 2004). Figure 3 shows a comparison of the vapour distributions in different Mars years in a region surrounding Gale crater. The distributions are broadly similar in different Mars years, though there are some differences related to the dust distribution. As the dust distribution for MY 26 best represents that for the periods in MY 31 and 32 that we are studying here (see Figure 4), we assimilate the TES vapour column data from MY 26. The vapour assimilation procedure is described fully in Steele et al. (2014b). The only difference here is that we also include the regolith model described earlier. The adsorbed water content of the regolith was initialised at each grid point to speed up the spin-up process. Values of 1 kg m^{-3}, 0.5 kg m^{-3}

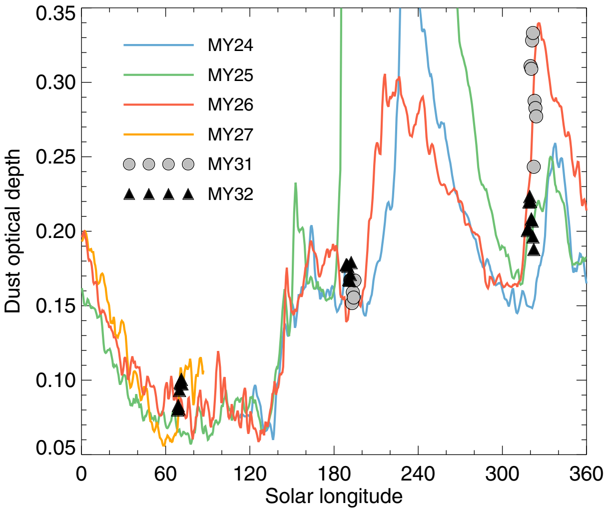

Figure 4: Variation of the infrared dust optical depth over Gale crater for multiple Mars years. Lines show the optical depth as determined from TES observations. Symbols show the optical depth for MY 31 and 32, corresponding to the periods covered in the simulations. These optical depths are derived from MCS and Thermal Emission Imaging System data (Montabone et al., 2015).

and 0.1 kg m^{-3} were used for simulations with the F71, J97 and Z97 isotherms respectively (corresponding to adsorbed values at ∼230 K; a mean daily temperature at Gale crater). Water is initially lost from the upper few centimetres of regolith to the atmosphere, but as vapour columns are being assimilated, the atmospheric vapour abundance remains in line with observations. By the end of the assimilations, the water distribution in the upper 10–15 cm of regolith in the region around Gale crater (the region which will interact with the atmosphere in the mesoscale simulations) reaches equilibrium, and a repeatable diurnal cycle occurs. Figure 5 shows a comparison between the TES water vapour column observations and the assimilation results around the three times of year the mesoscale simulations are performed.

3. Comparison with REMS data

Before we look at the water cycle both within Gale crater and in the surrounding area, we first compare the model predictions of pressure, temperature and wind with measurements from the REMS instrument. For each of the three periods we are investigating, REMS data are available for two different Mars years. These are MY 31 and 32 for the periods L_S = 187.8–193.1° and L_S = 319.8–325.0°, and MY 32 and 33 for the period L_S = 68.3–72.3°. Figure 6 shows the location of the Curiosity rover, compared to the closest mesoscale model grid points in domain 3, for the time periods we are investigating. As can be seen, the rover is closest to the grid point at the top right between MSL sols 67–496, and closest to the grid point at the bottom left between MSL sols 736–1164 (where MSL sol represents the number of sols since the Curiosity rover landed). In the mesoscale model, there are only

ACCEPTED MANUSCRIPT

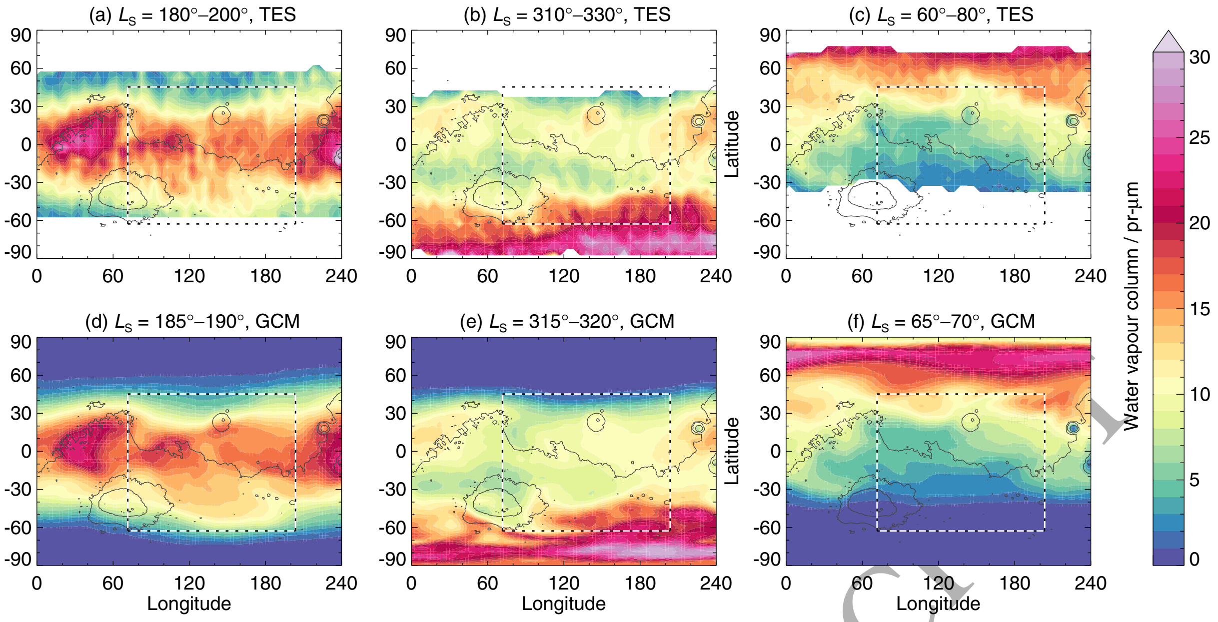

Figure 5: Comparison between the MY 26 water vapour distributions, normalised to 610 Pa, from (a–c) TES observations, and (d–f) GCM assimilation results for the three periods the mesoscale simulations are performed for. The parent domain is shown by the black and white rectangle. TES data are averaged over a longer time period (20° of L_S) than the GCM results (5° of L_S), to ensure there are enough observations for full longitudinal coverage. Black contours show topography.

small differences in the thermal inertia and albedo values between these two grid points, due to the spacecraft data being averaged over the 6 km grid boxes. The thermal inertias of the top-right and bottom-left grid points are 295 tiu and 292 tiu respectively, while the albedos are 0.234 and 0.226. In reality, there will be much more variation in surface properties. For example, Martínez et al. (2014) report thermal inertias ranging from 295 tiu on sol 82 to 452 tiu on sol 139. As such, it is unlikely that we will be able to exactly match the REMS observations, but good agreement in the diurnal cycle of temperature and pressure should be expected. As the model grid points have similar surface properties, we show temperature and pressure results from the top right grid point in Figure 6 (137.45°E, 4.59°S). Winds are shown for both the top right and bottom left grid points, as these have more variation. Detailed comparison of mesoscale model output with REMS pressure, temperature and wind measurements have been made by Pla-Garcia et al. (2016), and many of the same arguments presented there apply here. As such, we will only briefly discuss the comparisons, and reference should be made to Pla-Garcia et al. (2016) for more detailed discussions.

3.1. Pressure

Figure 7 (first column) shows a comparison between REMS pressure measurements and mesoscale model output for the three different periods studied. Each panel shows REMS measurements for six sols in two different Mars years, and six sols of mesoscale data. The daily-mean pressure value is controlled by the CO_2 cycle, and hence is inherited from the

ACCEPTED MANUSCRIPT

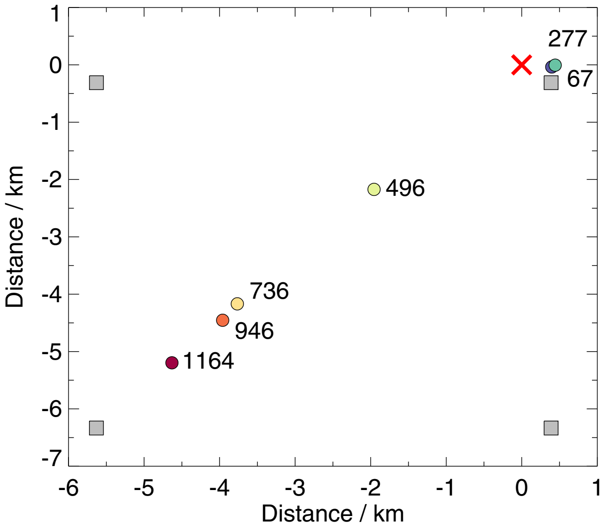

Figure 6: Location of the Curiosity rover on six different sols (coloured circles) in relation to the landing site (red cross). The grey squares show the four closest mesoscale model grid points. The sol numbers represent the number of sols since the Curiosity rover landed.

initial conditions provided by the GCM. In order to best match the observed pressure cycle, we perform the same procedure as Pla-Garcia et al. (2016), wherein a fractional adjustment is applied to the GCM pressure field. This fractional adjustment is determined by dividing the mean pressure from REMS measurements with the mean pressure from initial test mesoscale simulations. The adjustment factors for the periods shown in Figure 7(a,d,g) were 1.06, 1.01 and 1.02 respectively.

From Figure 7, the mesoscale model results appear to be consistent with the REMS data. The primary sources of diurnal pressure variations are atmospheric tides, and the amplitude of the tidal contribution to the pressure cycle is correlated with the opacity of the atmosphere (e.g. Guzewich et al., 2016). The amplitudes of the diurnal pressure cycles for the three periods shown, averaged over six sols, are 87, 107 and 59 Pa in the REMS measurements, and 88, 110 and 63 Pa in the mesoscale model, showing good agreement. The largest amplitude occurs during the $L_S = 321°$ period (Figure 7d), which is the dustiest of the three periods (see Figure 4). The pressure variation at $L_S = 321°$ is relatively smooth, and matched well by the mesoscale model, while in the other two periods more complex structure is visible in the REMS measurements. At some times this complex structure is captured by the model, while at other times (e.g. between 18:00–20:00 at $L_S = 189°$ and 23:00–02:00 at $L_S = 69°$) there are discrepancies between the model and REMS data. Similar discrepancies are evident in the simulations of Pla-Garcia et al. (2016), and may be caused by circulation patterns which are difficult to capture at the resolution used here.

3.2. Surface and atmospheric temperature

The middle column of Figure 7 shows comparisons between REMS surface temperature measurements and mesoscale model output for three different periods (the uncertainties in

ACCEPTED MANUSCRIPT

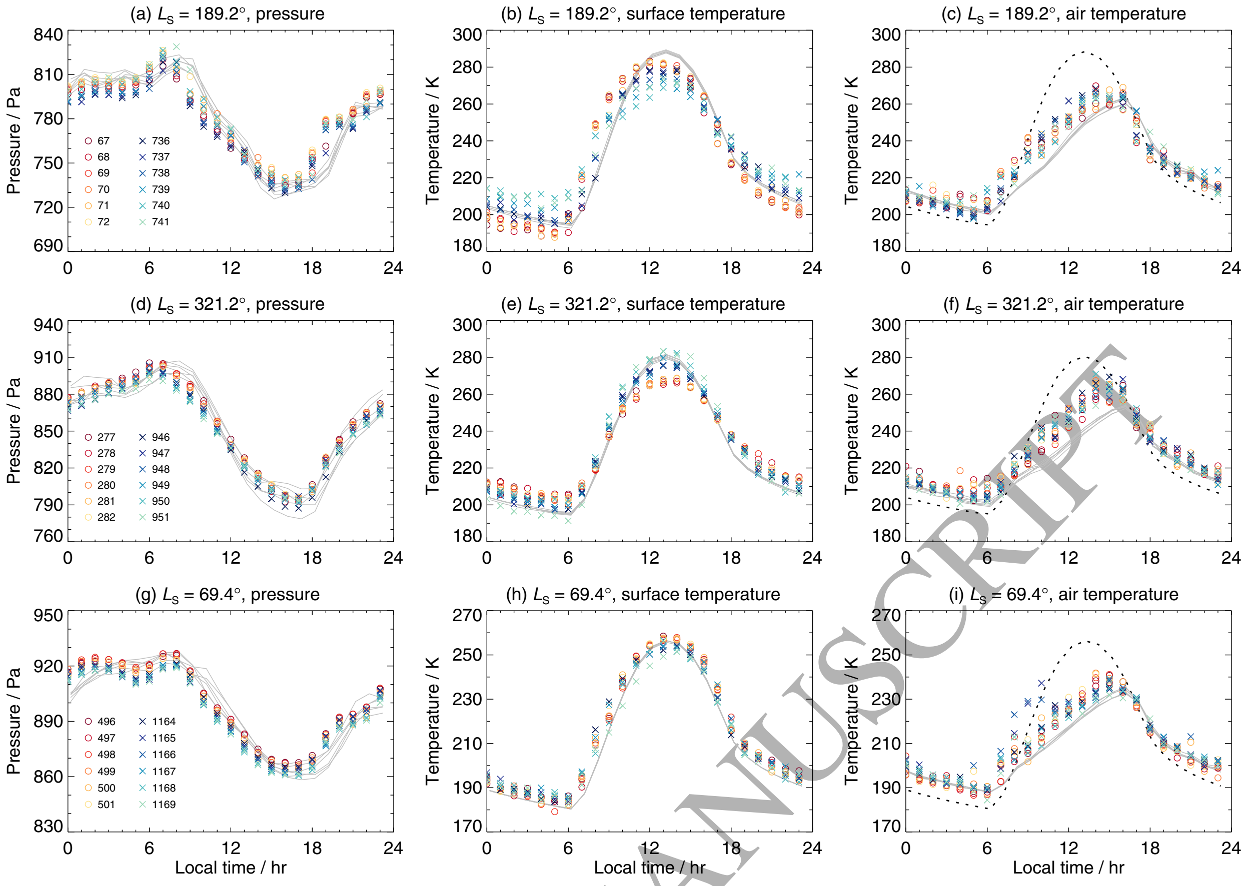

Figure 7: Comparison between REMS measurements (symbols) and mesoscale model predictions (lines) of pressure (left column) surface temperature (middle column) and air temperature (right column). Sol numbers represent the number of sols since the Curiosity rover landed. REMS data are shown for six sols, centred on the L_S value labelled above each plot. Model data are at altitudes ranging between 2.4–3.4 m, with REMS measurements at 1.6 m. The dashed black lines in the last column show the modelled surface temperature.

the REMS data are around 5 K). The REMS measurements in Figure 7(b,e) clearly show the effects of changing thermal inertia between the measurements taken at the same times of year in MY 31 (circle symbols) and MY 32 (cross symbols), with a higher thermal inertia resulting in warmer nighttime temperatures and cooler daytime temperatures. The mesoscale model surface temperatures compare well with the REMS data (particularly around $L_S = 321°$ and $L_S = 69°$), generally falling within the 5 K uncertainty, though as the surface properties are fixed the temperatures cannot match the variation seen between Mars years. Around $L_S = 189°$ (Figure 7b) the nighttime (18:00–06:00) surface temperatures in the mesoscale model fall between the REMS measurements from different Mars years. During the morning, the REMS surface temperatures increase more quickly than in the mesoscale model, while during early afternoon the peak surface temperatures in the mesoscale model are around 10 K too warm. Similar features were noted by Pla-Garcia et al. (2016), and may be the result of topographic orientation, or discrepancies in the thermal inertia, albedo or dust opacity.

The last column of Figure 7 compares atmospheric temperatures. The REMS mea-

ACCEPTED MANUSCRIPT

ACCEPTED MANUSCRIPT

surements are made at a height of ∼1.6 m above the surface, and we use the ambient air temperature values from the PDS. The mesoscale model results are from the lowest model layer, which varies in height with time of day as well as season. The layer midpoint is lowest at 06:00, where the height ranges from 2.4–2.6 m depending on season (with the lowest heights around $L_{\mathrm{S}} = 68.3$–72.3°, and the greatest heights around $L_{\mathrm{S}} = 187.8$–193.1°). The midpoint is highest at 16:00, where the height ranges from 3.0–3.4 m. As such, when comparing temperatures with REMS data, the mesoscale model temperatures correspond to altitudes around 1 m higher during the night, and 1.5–2 m higher during late afternoon.

As was the case for surface temperatures, there is generally good agreement between REMS air temperature measurements and mesoscale model output during the night (18:00–06:00) in all three seasons. During the daytime, the mesoscale model results can be 10–15 K cooler than the REMS measurements, eventually reaching agreement by around 16:00–17:00. Taking into account the difference in height between the REMS measurements and mesoscale output, the temperature differences correspond to daytime lapse rates of around 5–7 K m^{-1}. Superadiabatic lapse rates of this magnitude have been observed by Mars Pathfinder and the Mars Exploration Rovers (Schofield et al., 1997; Smith et al., 2004), so the mesoscale model temperatures are consistent with observations. REMS measurements often show variations associated with turbulent eddies, but due to the 6 km grid box sizes these cannot be captured by the mesoscale model (this would require large-eddy simulations), and the temperature variations in the model are generally a lot smoother.

3.3. Wind

Due to damage to one of the wind sensors, determination of the wind speed and direction from REMS data is difficult, and under the best conditions (temperatures above 213 K with wind blowing towards the front of the rover) the uncertainty is ∼50% for the wind speed, and ∼20° for direction (Gómez-Elvira et al., 2014). Additionally, the winds in the lowest layer of the mesoscale model correspond to altitudes around 1.5–2 m higher than the REMS wind sensor, and the results are averages over 6 km grid boxes. Nevertheless, for completeness, Figure 8 shows a comparison between the REMS measurements and mesoscale model predictions of wind speed and direction. REMS measurements are plotted for different Mars years, with faintly coloured lines representing observations which may be unreliable due to electronic noise, the wind sensor not being correctly configured, or a wind blowing towards the rear of the rover. Mesoscale model data are plotted for two different grid points.

Looking at the mesoscale data first (panels d–f) it is clear that there is a general trend in all three periods for the wind to have a southerly component from 17:00–07:00 and a northerly component from 08:00–16:00, associated with downslope and upslope flows along Mount Sharp. Tyler and Barnes (2015) noted that around these two times of day (08:00 and 17:00), the mass flux of air into craters reverses sign. The wind between 17:00–07:00 tends to be southerly or southeasterly in all three periods. Between 08:00–16:00, there are differences

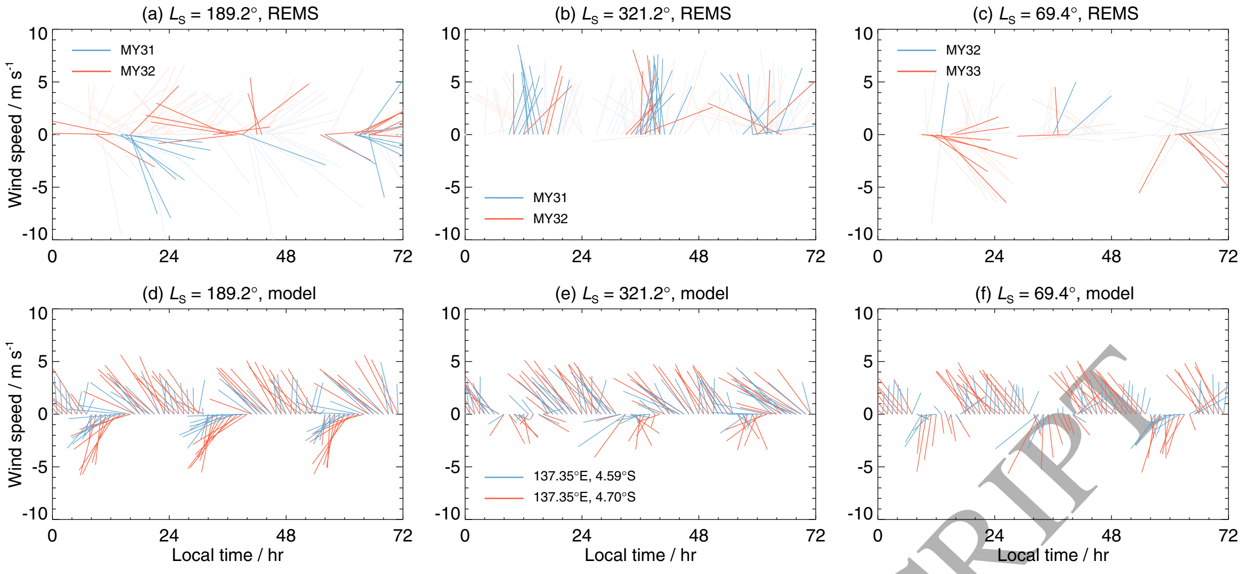

Figure 8: Stick plots showing wind speed and direction from (a–c) REMS measurements, and (d–f) the mesoscale model. The length of each stick represents speed, and the angle represents the incoming direction of the wind, defined as clockwise with respect to the north. Results are shown for three sols centred on the labelled L_S values. REMS data from two Mars years are shown with different coloured lines. Faint lines show data that may be unreliable. Mesoscale results from two different grid points are shown with different coloured lines. REMS data are for an altitude 1.6 m, while model data range between 2.4–3.4 m.

in the behaviour of the wind in the three periods. Around $L_S = 189°$ (Figure 8d) the wind veers from a northerly to an easterly, while around $L_S = 321°$ and $L_S = 69°$ (Figure 8e,f) the winds tend to vary from northwesterly to northeasterly, though with periods of southerly or south-easterly winds.

As noted earlier, it is difficult to compare 6 km average winds with those recorded at a single point, which will show much greater fluctuation. At around $L_S = 189°$, the model shows some agreement with the REMS data. Between 12:00–16:00, the REMS winds on the first two sols are in a west-northwest direction (Figure 8a), which is similar to the model results between ~15:00–17:00. At other times of day there is less agreement, but it can be seen by comparing winds at similar times of day in different Mars years how varied they can be. Around $L_S = 321°$ the REMS data show winds ranging from west-southwesterly to east-southeasterly (Figure 8b), which is in general agreement with the model. The REMS data do not show any winds with a northerly component like those in the model between 08:00–16:00. Around $L_S = 69°$ the number of REMS measurements is again low (Figure 8c), but some agreement with the model is seen. For example, between 09:00–13:00 on the first sol, and 12:00–16:00 on the third sol, the wind has a northerly component, as in the model. The winds at other times range from west-southwesterly to south-southeasterly, which is similar to the modelled winds.

In terms of wind speed, the agreement is generally good, and within the ~50% uncertainty of the REMS measurements. However, there are some periods where the REMS

ACCEPTED MANUSCRIPT

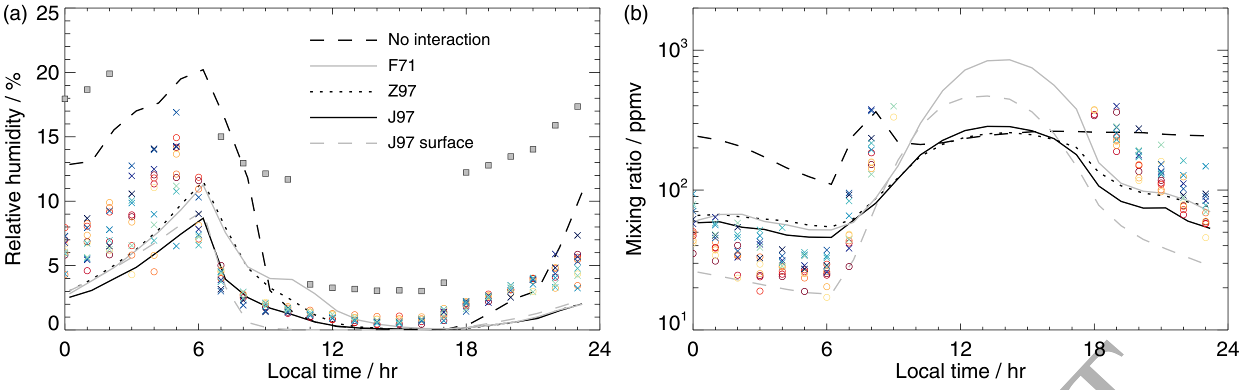

Figure 9: Comparison between REMS data (symbols) and mesoscale model predictions (lines) of (a) relative humidity (RH), and (b) volume mixing ratio (vmr). REMS data are shown for six sols in two different Mars years, covering the period $L_S = 187.8$–$190.7°$ (see Figure 7 for sol numbers). The grey squares in (a) show the RH uncertainty, which is around 2–10%. Mesoscale results are shown for no regolith-atmosphere interaction, and for the F71, Z97 and J97 adsorption isotherms. Mesoscale results are averaged over six sols, to make the figure clearer, and correspond to altitudes ranging from 2.4–3.4 m. The 'J97 surface' results show the RH and vmr at the surface-atmosphere boundary from the simulation using the J97 isotherm.

measurements are around 8–10 m s^{-1} while the wind speeds in the model are around 2–3 m s^{-1} (e.g. some of the measurements in the first two sols of Figure 8a and the first sol of Figure 8c). These may be caused by turbulent wind gusts, which cannot be captured at the 6 km resolution of the model.

The comparisons of pressure and temperature shown here suggest the mesoscale model is successfully capturing the main features of the Gale crater circulation. The wind comparison shows that the broad characteristics of the mesoscale circulation are correct, though it is not possible for the model to resolve the short-term fluctuations of winds that can be seen in the REMS data. With confidence that the model is capturing the true nature of the mesoscale circulation, we now go on to look at the water cycle in and around Gale crater at three different times of year.

4. The water cycle in southern hemisphere early spring

4.1. Comparison with REMS measurements

First we look at southern hemisphere spring ($L_S = 187.8$–$193.1°$), which is when vapour columns in the Gale crater region are at their largest for the year (~15 pr-μm) due to transport of vapour from the subliming north polar ice cap (Smith, 2004). Figure 9 shows a comparison of relative humidity (RH) and water vapour volume mixing ratio (vmr) between REMS measurements and the model output. Again, it must be remembered that the REMS measurements are at an altitude of ~1.6 m, while the model values correspond to altitudes ranging from 2.6–3.4 m, and so there are likely to be differences in the temperatures and water vapour values. Additionally, REMS vmr measurements are only shown when they are less than 400 ppmv, as values above this are unreliable.

ACCEPTED MANUSCRIPT

Compared to REMS RH measurements, the simulation with no regolith-atmosphere interaction appears too wet between around 23:00–09:00 (Figure 9a). The vmr, which varies between 100–200 ppmv between 00:00–06:00, is also larger than determined from REMS measurements (Figure 9b), which has mean values varying between 30–60 ppmv. (Note that REMS vmr values are not measured, but determined from RH, temperature and pressure measurements.) The diurnal variation of vmr is also markedly different than that determined from REMS, with the peak value occurring at around 08:00, a relatively constant vmr for much of the day thereafter, and a slow early morning decrease, due to condensation onto ground frost. The early morning peak is due to the sublimation of surface ice, and is similar to the behaviour seen in some Phoenix TECP measurements (Zent et al., 2016). A better agreement with the REMS measurements is achieved when including the regolith diffusion model. The J97 isotherm best matches the decrease in RH between 06:00–10:00, though the vmrs between 00:00–06:00 are larger than those determined from REMS measurements. This is similar to the results of the 1D simulations of Savijärvi et al. (2016). However these vmrs correspond to an altitude of $\sim$2.6 m. At the atmosphere-surface boundary, the vmrs between 00:00–06:00 are lower than those determined from REMS measurements (only the J97 results are shown for the atmosphere-surface boundary, to make the plot clearer). As the REMS sensor height falls in between these two altitudes, the model results are consistent with the measurements.

While the vmr values in the lowest atmospheric layer and the surface bound the REMS measurements, the RH values for both cases are on the lower end of the REMS measurement range. However, the RH is very sensitive to the temperature in the cold nighttime conditions. For example, assuming the vmr values in the model are correct, then a temperature reduction of around 5 K between 00:00–05:00 increases the RH by around 3.5–4.5%, bringing the values in line with REMS data. Thus, while there are differences present, they do not signify a large departure from reality in the model. The F71 simulation has the largest daytime vmr value, while the values in the J97 and Z97 simulations are similar. This is because the F71 isotherm holds more adsorbed water than the other isotherms (see Figure 10), and there are therefore larger fluxes of vapour in and out of the regolith over the course of a sol.

From around 17:00–00:00, the REMS measurements show RH increasing more quickly than in the simulations which include the regolith diffusion model. As the vmr values are determined from the RH, these are also larger than in the model. Looking at Figure 7(a–c), the temperatures and pressures are generally in good agreement between REMS and the model. Thus, if correct, the higher RH and vmr values in the REMS data suggest a wetter atmosphere in the late evening than in the model. This may be due to vapour diffusing into the regolith more slowly than the model predicts, or due to peak daytime vapour abundances being larger than in the model. However, the RH values at this time have large uncertainties, and so both the REMS RH and vmr values may be too high. A similar disagreement between model results and REMS vapour mixing ratios over the 17:00–00:00 period occurs in the 1D

ACCEPTED MANUSCRIPT

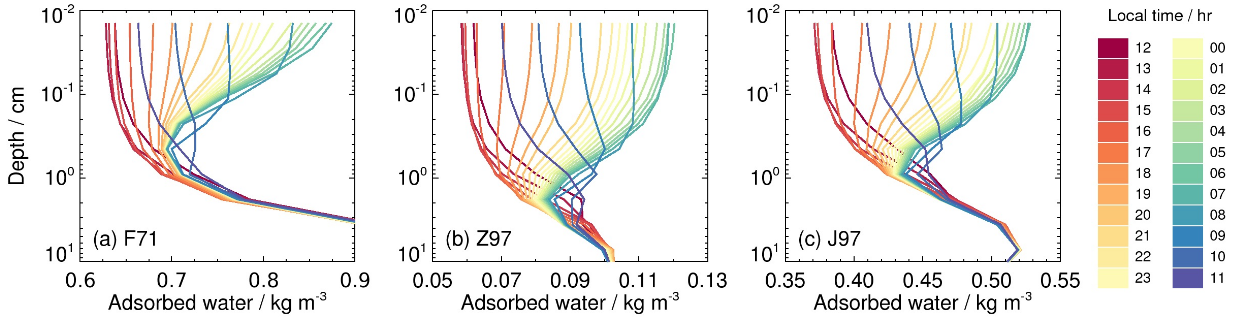

Figure 10: Diurnal variation of water adsorbed onto regolith grains at the Curiosity rover location at $L_S = 189°$. Results are shown for three simulations with different adsorption isotherms (see text for details).

simulations of Savijärvi et al. (2016).

In terms of the spatial distribution of water in and around Gale crater, the results are similar in all the simulations that include water vapour exchange with the subsurface. It is largely just the amount of water vapour in the atmosphere that differs slightly. Thus, we use the results of the simulation with the J97 adsorption isotherm, along with those from the simulation with no regolith-atmosphere interaction, to look in more detail at the behaviour of vapour in and around Gale crater. First we describe the diurnal variation of the vapour distribution for the case of no regolith-atmosphere interaction, and then we see how diffusion into and out of the regolith affects the vapour distribution.

4.2. The water distribution without regolith-atmosphere interaction

Figure 11 shows the vapour distribution as a function of both latitude-altitude (panels a–d) and longitude-altitude (panels e–h) at $L_S = 189°$. These cross sections pass through the location of the Curiosity rover, which is marked with a grey triangle. The vapour distribution varies on different sols, due to the transport of vapour from regions surrounding Gale crater, but the behaviour shown in Figure 11 is representative of the sols in this period. As well as these cross-sections, Figure 12 shows the temperature and wind in the lowest model layer at six different times of day.

Vapour is generally well mixed in the lowest few kilometres of the atmosphere by late afternoon (Figure 11a,e). At this time, the large-scale flow in the lowest few kilometres of the atmosphere over the dichotomy boundary is upslope in a deep layer, i.e. from north to south (see Figure 13a). This is in the same direction as the mean surface winds in the lower branch of the Hadley cell at this time (Figure 14a). As such, the meridional flow within Gale crater is also generally in a southwards direction (Figure 11a, Figure 12a). However, the upslope winds on the northern crater wall are opposite to the generally southwards flow, and result in a convergence boundary on the north crater rim (Figure 12a). The wind in the zonal direction is weaker than in the meridional direction. At the east and west crater walls there are mesoscale upslope flows, while the return flow, due to the conservation of mass, results in downslope winds over Mount Sharp (Figure 11e).

ACCEPTED MANUSCRIPT

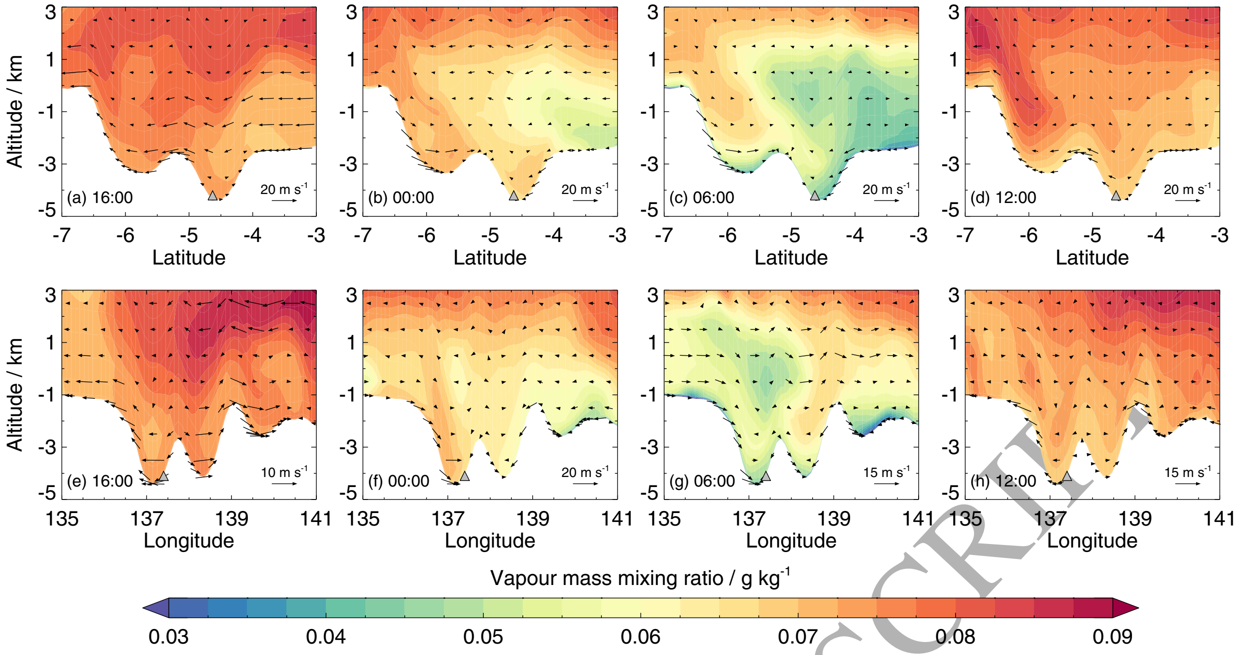

Figure 11: Water vapour distribution at four different local times, as a function of (a–d) latitude and altitude, and (e–h) longitude and altitude. Vectors show the magnitude and direction of the wind in the plane of the image. Results are from a simulation with no regolith-atmosphere interaction, and are for $L_S = 189°$. The local times correspond to those at the Curiosity rover location (grey triangle). White shading shows topography.

ACCEPTED MANUSCRIPT

By midnight the atmosphere has cooled, and downslope (katabatic) flows develop more widely (Figure 12c). As the large-scale flow across the dichotomy boundary has advected drier near-surface air from the north towards Gale crater, the transport of vapour downslope is larger on the southern crater wall (Figure 11b). In the zonal direction, the near-surface vapour abundance to the east of Gale crater has been reduced by surface ice formation, so downslope winds on the western crater wall transport more vapour to the crater floor (Figure 11f).

By 06:00 the large-scale flow across the dichotomy boundary has changed direction, and is now flowing downslope near the surface, from south to north (Figure 13d), which is in the opposite direction to the mean surface winds in the lower branch of the Hadley cell (Figure 14a). These winds occur over a much smaller vertical range (∼1 km compared to 3–4 km at 18:00). As the slope of the southern crater wall is in the same direction as the slope of the dichotomy boundary (and hence the same direction as the prevailing wind) the downslope flows are strongest here (Figure 11c, Figure 12d). However, the near-surface vapour abundance has been depleted due to the formation of surface ice around the rim of the crater, so little vapour is transported into the crater. Additionally, as noted by Rafkin et al. (2016), the air flowing down the crater walls tends to flow over the cold air on the crater floor. Near-surface vapour amounts at the base of the crater at 06:00 are around half their value at 17:00. The downslope winds continue in the zonal direction, with the formation of

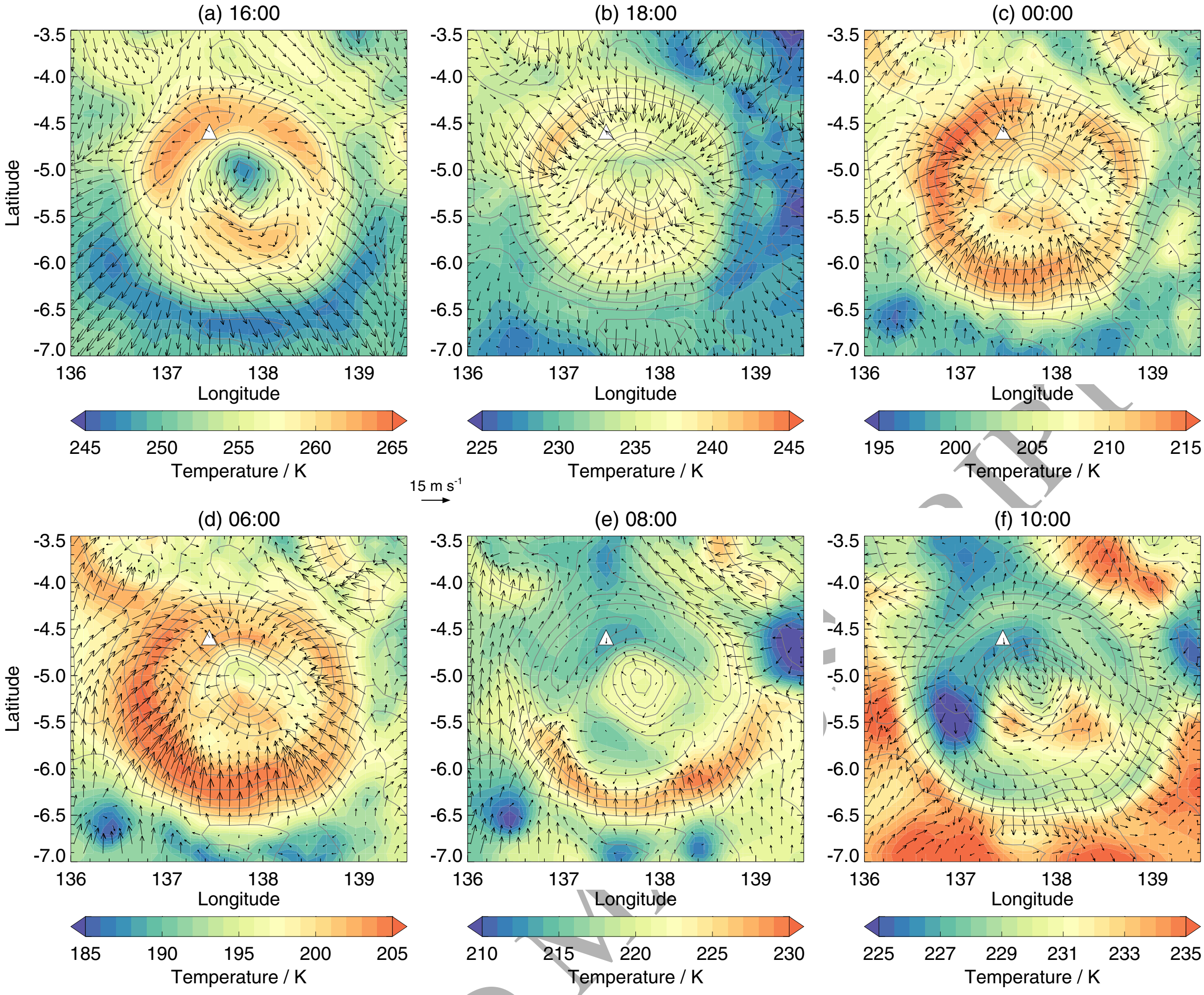

Figure 12: Temperatures (shading) and winds (vectors) in the lowest atmospheric layer for 6 different times of day at $L_S = 189°$. Note the temperature range changes with each plot. Grey contours show heights above the areoid.

surface ice outside the crater again depleting the near surface of vapour (Figure 11g).

At 08:00 there are still downslope flows on the southern crater wall (Figure 12e), but by 10:00 the atmosphere has warmed and upslope flows develop (Figure 12f). By midday, these upslope flows advect relatively dry air from the crater floor up the sides of the crater, which then mixes into the atmosphere around the crater rim (Figure 11d,h). At this time, the large-scale dichotomy boundary flow is again upslope, from north to south, and as such the mesoscale upslope flow on the southern wall of Gale crater is stronger than on the northern crater wall. Daytime mixing continues, until the vapour distribution again resembles that in Figure 11a,e. The near-surface circulation at $L_S = 189°$ is in good agreement to that at $L_S = 180°$ in the work of Rafkin et al. (2016), and at $L_S = 151°$ in the work of Tyler and Barnes (2013).

ACCEPTED MANUSCRIPT

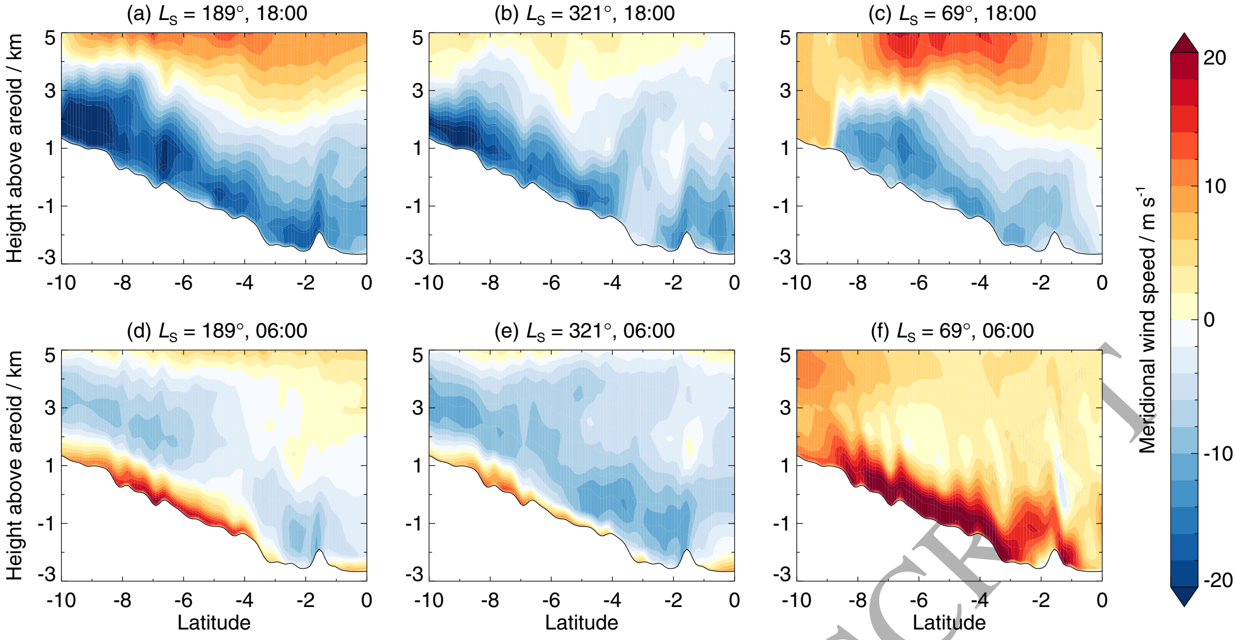

Figure 13: Meridional winds along the dichotomy boundary at 135.7°E (to the west of Gale crater); see Figure 1. Results are shown for three different periods at local times of (a–c) 18:00, and (d–f) 06:00. A positive wind speed occurs when the wind is blowing from south to north (i.e. downslope). Black contours show topography.

4.3. The water distribution with regolith-atmosphere interaction

We now look at the effect that including regolith-atmosphere interaction has on the water distribution, as this was shown in Section 4.1 to lead to better agreement with REMS RH and vmr data. Figure 15 shows results in the same format as Figure 11, but for the simulation using the J97 adsorption isotherm. The temperature, pressure and circulation are exactly the same between the runs both with and without regolith-atmosphere interaction, as vapour has little impact on the thermal structure of the atmosphere in the small abundances present.

At 16:00 the vapour is well mixed in the lowest few kilometres (Figure 15a,e). By midnight, the near-surface vapour abundance (particularly in the lowest few hundred metres) is reduced when including regolith-atmosphere interaction (compare Figure 15b,f with Figure 11b,f). In the near-surface layer at the location of the Curiosity rover (at a height of ∼2.7 m), the vapour mass mixing ratio is around 3.5 times smaller than when ignoring regolith-atmosphere interaction, with a value of ∼28 mg kg^{-1} (66 ppmv) compared to ∼100 mg kg^{-1} (242 ppmv). The flux of vapour into the regolith is greater on the upper slopes of the crater walls, and decreases in magnitude while approaching the crater floor. This can be seen in Figure 16, which shows the flux of vapour out of the regolith (panels a–c) and the vapour mass mixing ratio at 40 m above the surface (panels d–f) for three different times of day.

The flux at 00:00 is greatest on the southern crater wall, where vapour diffuses into the

ACCEPTED MANUSCRIPT

ACCEPTED MANUSCRIPT

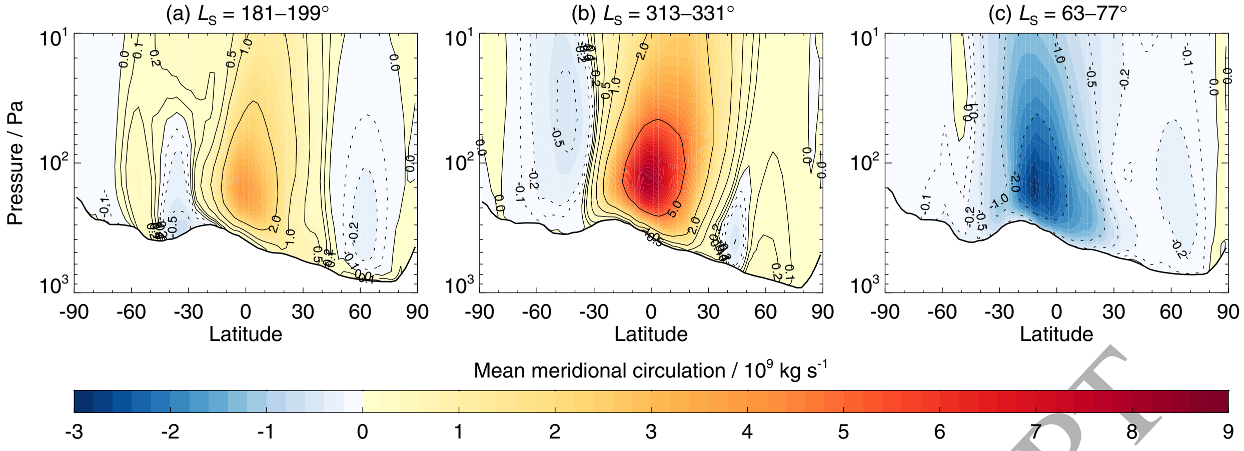

Figure 14: Mean meridional circulation in the lower atmosphere over three 30-sol periods. Results are from the GCM simulations used for the mesoscale initial and boundary conditions. Blue shading and dotted contours represents anticlockwise circulation. Red shading and solid contours represents clockwise circulation. White shading shows zonally-averaged topography.

regolith at a rate of 2–3 pr-μm sol^{-1} (Figure 16a). The flux is largest here at this time as the vapour values are large (see Figure 15b) and the near-surface winds are strong, resulting in increased turbulence. This can be seen in the parameterization of the flux of vapour from the surface to the atmosphere, which is determined via a balance of the fluxes at the regolith-atmosphere boundary: $F_{\mathrm{atm}} = -F_{\mathrm{reg}}$. For the atmosphere, the flux is $F_{\mathrm{atm}} = \rho k_{\mathrm{atm}}(q_1 - q_{\mathrm{b}})$, where the subscript '1' represents the first atmosphere layer, the subscript 'b' represents the regolith-atmosphere boundary, q is the water vapour mass mixing ratio in the atmosphere and ρ is the atmospheric density at the surface. The coefficient is given by $k_{\mathrm{atm}} = C_{\mathrm{h}}|\mathbf{u}|$, where C_{h} is the wind-dependent scalar transfer coefficient and $|\mathbf{u}|$ is the magnitude of the near-surface wind (for full details see Steele et al., 2017). As the strength of the wind increases, near-surface turbulence mixes the vapour distribution, resulting in larger vapour abundances close to the surface than would be the case for stable conditions. This allows more vapour to diffuse into the regolith.

Vapour continues to diffuse into the regolith during the night, with the near-surface atmosphere above the floor of Gale crater becoming increasingly depleted of vapour. The majority of the vapour becomes adsorbed onto regolith grains. By 06:00 the vapour mass mixing ratio at the location of the Curiosity rover is 20 mg kg^{-1} (50 ppmv), compared to 40 mg kg^{-1} (100 ppmv) when ignoring regolith-atmosphere interaction (see Figure 9b). As the dichotomy boundary flow at this time is downslope, i.e. from south to north, more vapour is advected into Gale crater down the southern crater wall (Figure 15c). Downslope winds on the southern wall of the crater have strengthened compared to at 00:00, so there is increased vapour flux into the regolith (Figure 16b). As Curiosity is located at the base of Mount Sharp it is affected by nighttime downslope flow, but this flow is relatively weak, and vapour abundances above Mount Sharp are relatively small during the night (see Figure 15). As

ACCEPTED MANUSCRIPT

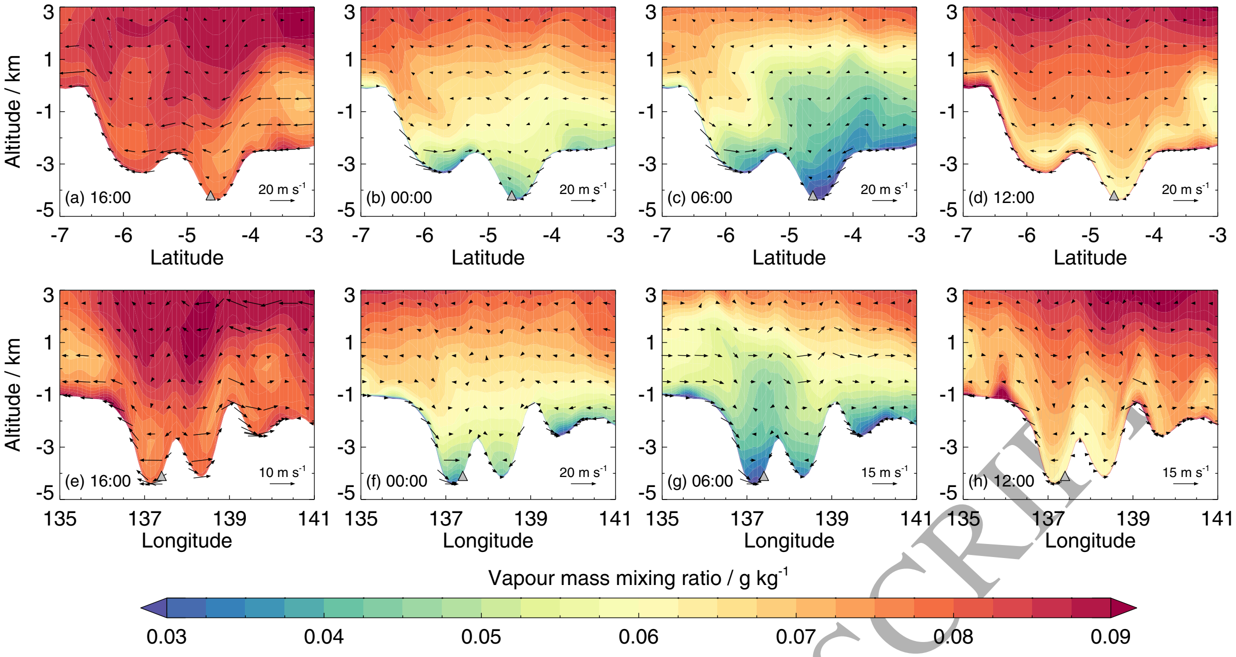

Figure 15: As Figure 11, but for a simulation with regolith-atmosphere interaction using the J97 isotherm.

such, little vapour is transported in this flow, and the vapour abundance at the Curiosity location is only a few percent larger than that a few kilometres away at the lowest point of the crater floor. This difference increases to $\sim$20% at 40 m above the surface (Figure 16e).

Vapour continues to diffuse into the regolith until around 09:00, when the rapidly-warming atmosphere and subsurface results in a large flux of vapour out of the regolith (due to desorption of vapour from the regolith grains). By 12:00, this flux is strongest on the southern crater wall (Figure 16c) as the relatively strong upslope winds act to transport the vapour away, allowing more to diffuse out of the regolith. By midday, vapour is diffusing out of the regolith at a rate of around 4–5 pr-μm sol^{-1}. This results in a three-layer structure in the vapour distribution (Figure 15d,h). Close to the surface there are relatively large vapour abundances caused by the vapour diffusing from the regolith. This vapour is generally in the lowest tens of metres, but can extend to a few hundred metres at convergence boundaries (such as to the west of Gale crater in Figure 15h). Above this is a drier layer, extending a few kilometres in height, caused by the advection of dry air from within the crater by the daytime upslope winds. Above the drier layer, the vapour values increase again. Anabatic winds have previously been shown to transport vapour from the base of Olympus Mons to above the caldera (Michaels et al., 2006; Spiga and Forget, 2009), but while the transport mechanism here is the same, the source of the vapour is not. Here, the vapour has diffused out of the regolith during the day (due to desorption in the warmer daytime temperatures), rather than pre-existing at lower levels. The three-layer structure remains for the next few hours, until eventually daytime mixing brings the vapour distribution back to that seen at 16:00 in Figure 15a,e).

ACCEPTED MANUSCRIPT

ACCEPTED MANUSCRIPT

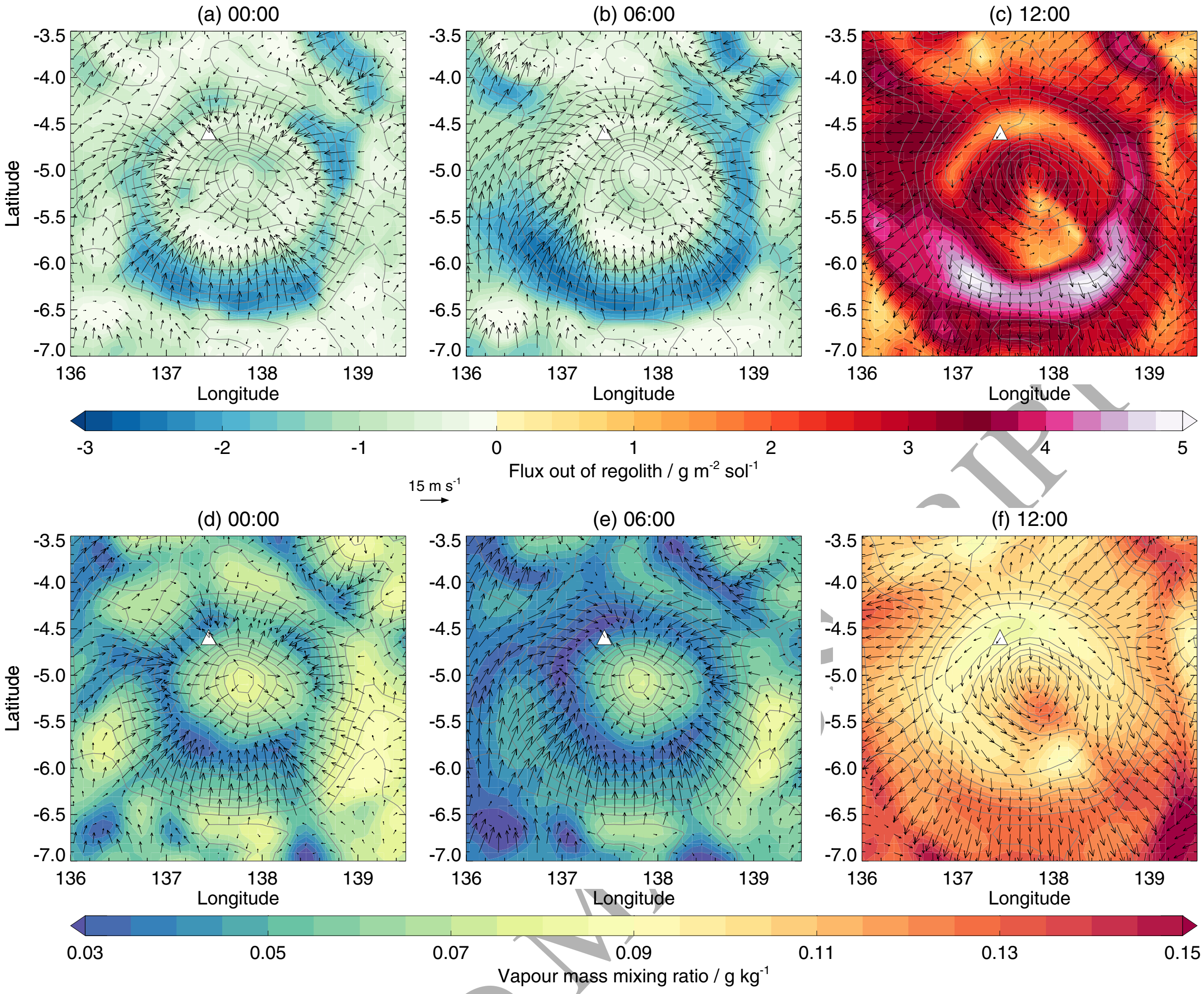

Figure 16: (a–c) Water vapour flux out of the regolith, and (d–f) water vapour mass mixing ratios at an altitude of 40 m, for three different local times of day. Data are from the simulation using the J97 adsorption isotherm, and are for $L_S = 189°$. Vectors show the wind in the lowest model layer, and grey contours show heights above the areoid. Local times correspond to those at the location of the Curiosity rover (white triangles).

Between 00:00–12:00 there is little cloud cover, but from 12:00 clouds begin to build, and are thickest between around 15:00–20:00 (Figure 17). Infrared absorption-only optical depths vary between 0.03–0.08. As the clouds are present during the day, they have the ability to reduce surface temperatures through a reduction in the radiation reaching the ground (though in these simulations clouds are not radiatively-active). However, Wilson et al. (2007) showed that clouds with infrared absorption-only optical depths of ∼0.2–0.4 are required to reduce daytime surface temperatures by 2–5 K. The cloud optical depths here are at least 2.5 times lower than this, and hence little reduction in surface temperature is expected.

There is typically a single cloud layer present, with its base varying between 30–40 km, depending on time of day. There is also sometimes a two-layer structure visible, with the base of the upper layer at around 40 km, and a lower layer ∼5 km thick centred around 30 km.

ACCEPTED MANUSCRIPT

ACCEPTED MANUSCRIPT

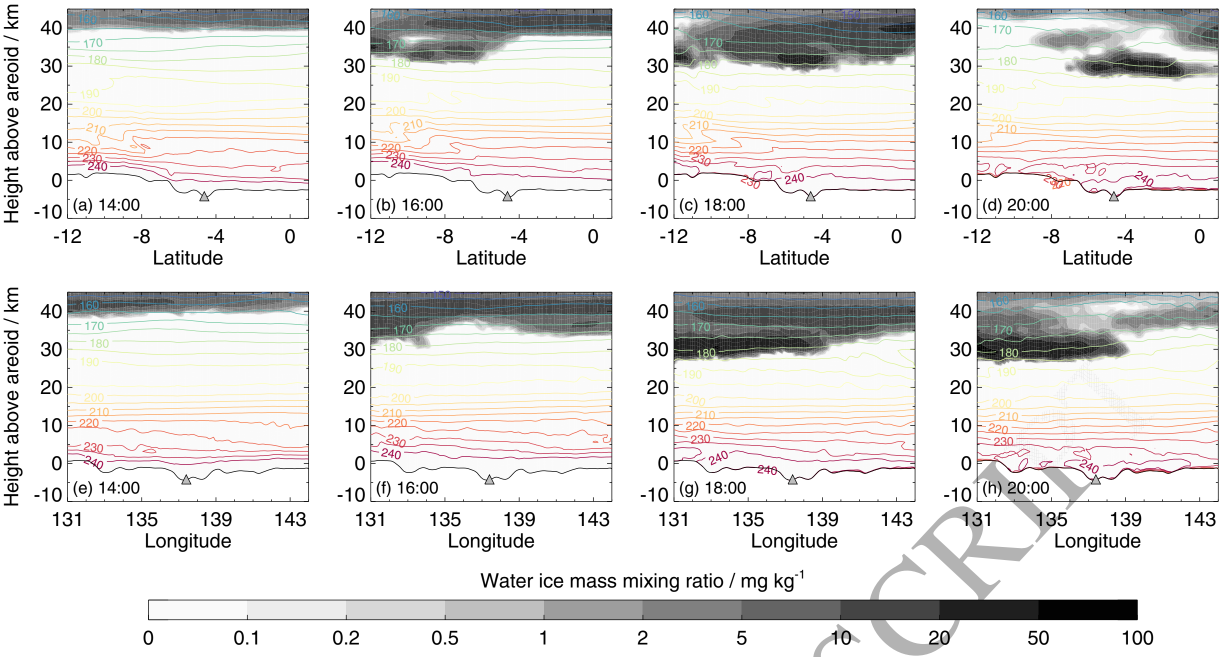

Figure 17: (a–d) Latitude-altitude, and (e–h) longitude-altitude cross sections showing ice clouds (shaded) and temperature (coloured contours) at four different times of day. Black contours show topography. Results are from a simulation with regolith-atmosphere interaction using the J97 adsorption isotherm, and are for $L_S = 189°$. The local times correspond to those at the Curiosity rover location (grey triangle).

Such a two-layer structure has been observed in NavCam images from the Curiosity rover, as well as in MCS observations (Moores et al., 2015). The ice particles are generally ∼2–4 μm in size, and are consistent with values determined from spacecraft observations (Clancy et al., 2003; Glenar et al., 2003; Madeleine et al., 2012). The peak opacities of the clouds (infrared extinction opacity per kilometre) range from 10^{-2} between 20–30 km, to $10^{-3.5}$–$10^{-2.5}$ at ∼40 km. While these clouds are likely to have little effect on surface temperatures, they have the ability to locally heat the atmosphere both at and above cloud-forming height by ∼5–15 K sol^{-1} (Steele et al., 2014a), which may have an impact on circulation patterns over Gale crater.

While the discussion above has focused on Gale crater, the same features (nighttime diffusion of vapour into the regolith on crater walls, dry nighttime crater floors and diffusion out of the crater walls during the morning and afternoon) are ubiquitous for the different sized craters in the mesoscale domain. This can be seen in Figures 18 and 19, which show the flux of vapour out of the regolith and the vapour mass mixing ratio at 100 m above the surface respectively, at eight local times of day. In the afternoon, there are increased vapour abundances in the afternoon, corresponding to the locations of crater walls, hilltops and other topographic features (Figure 19b,c). These increases are caused by vapour diffusing out of the regolith (Figure 18b,c), being advected up crater walls by upslope winds, and then being transported upwards at convergence boundaries. Eventually this vapour is advected by the large-scale horizontal winds (Figure 19d), which in this case are northerly winds

ACCEPTED MANUSCRIPT

flowing up the dichotomy boundary. During the late evening and night it can be seen that crater floors become drier than their surroundings (Figure 19e–h). This is due to diffusion of vapour into the regolith on the crater floors themselves, and a lack of vapour being transported in downslope flows, as the water diffuses into the regolith along the crater walls and becomes adsorbed onto the regolith grains (Figure 18e–h).

In terms of the overall loss or gain of subsurface water, Figure 20 shows the change in the total subsurface water content over the last five sols of the simulations for each period. Looking at the results for southern hemisphere early spring (Figure 20a) it can be seen that in general mass is being lost from the subsurface. This is because the regolith was initialised with output from a GCM, which cannot account for the small-scale circulation patterns and temperature variations resolved by the mesoscale model, which affect transport of water in and out of the regolith. The mass loss is greatest on crater floors as little water is available here during the night to diffuse into the regolith (see Figures 18 and 19). The maximum mass loss over five sols is $\sim$0.15 pr-μm, which is around one hundredth of the atmospheric water vapour column value at this time. As noted earlier, this vapour diffuses out of the regolith during the afternoon, and is transported away by the wind. Thus, this should not affect the comparison with REMS RH and vmr data, which is focussed on nighttime measurements.

Regions around the rims of craters, and around the raised topographic features to the north and east of Gale crater, experience either smaller amounts of mass loss, or mass gain. These are the regions where strong nighttime winds increase the flux of vapour into the regolith. This vapour diffuses down to depths of $\sim$5–10 cm, and becomes adsorbed onto the regolith grains. At these depths, the diurnal temperature variation is greatly reduced compared to at the surface, and so less of the water diffuses back to the surface during the day, and the mass of water at depth increases.

Regolith-atmosphere interaction also has an effect on the formation of surface ice. Figure 21 shows the maximum depth of surface ice, in microns, over the course of one sol at $L_{\mathrm{S}} = 189^\circ$. When regolith-atmosphere interaction is ignored (Figure 21a) surface ice forms in most locations during the night, except those with relatively high thermal inertia values (> 315 tiu). In these regions the nighttime temperatures are $\sim$10 K warmer than in the surrounding areas, which prevents the formation of surface ice. When regolith-atmosphere interaction is included, the depletion of vapour in the near-surface atmosphere (through diffusion into the regolith and adsorption onto regolith grains during the evening and night) greatly reduces the extent of surface ice cover (Figure 21b). Now there is no surface ice on the floor of any craters, though ice does form in the early morning on the eastern walls of the Lasswitz and Wien craters (to the south of Gale crater). The main area of surface ice is to the east of Gale crater, as vapour values are higher in this region (see Figure 3a–c). The distribution of subsurface ice is also limited to a few locations to the south and east of Gale crater (Figure 21c). Only small values of ice form at depths of a few millimetres below the surface, and sublime completely during the day.

ACCEPTED MANUSCRIPT

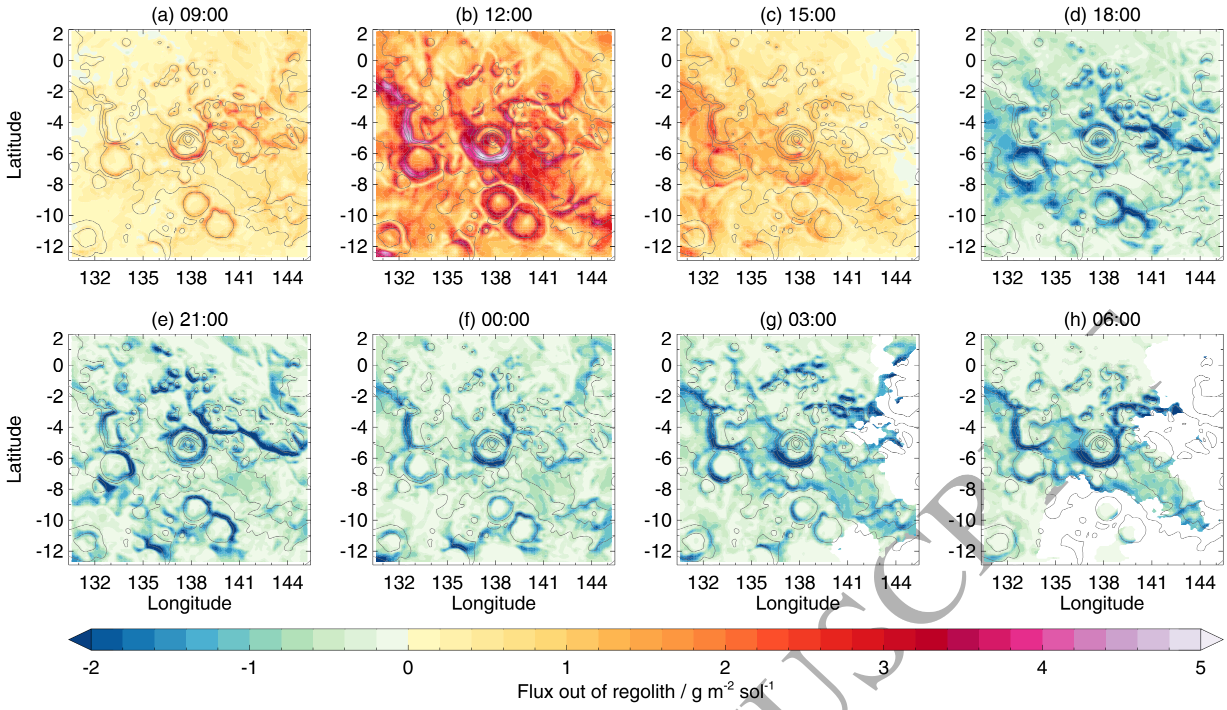

Figure 18: Diurnal variation of the flux of vapour out of the regolith in an area centred on Gale crater. Results are shown over one sol at $L_S = 189°$. The local times are given for the location of the Curiosity rover. White shading shows where surface ice has formed, which stops vapour transport between the regolith and atmosphere.

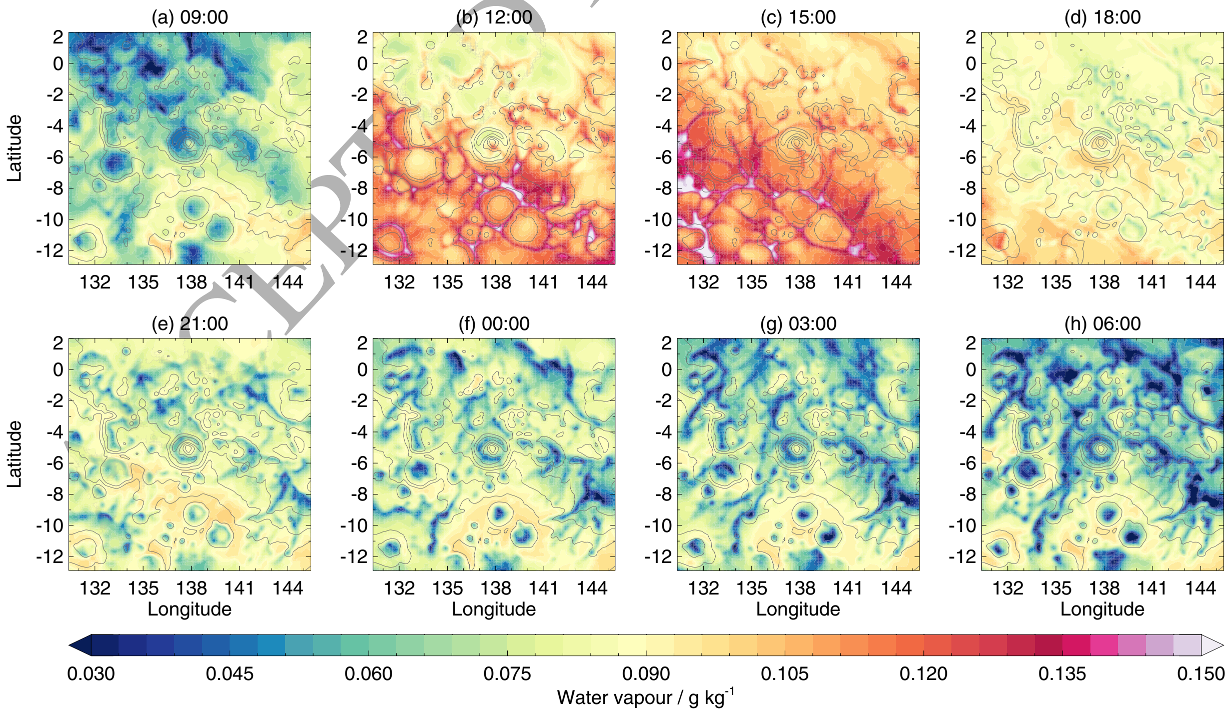

Figure 19: As Figure 18, but for the diurnal variation of water vapour at 100 m above the surface.

ACCEPTED MANUSCRIPT

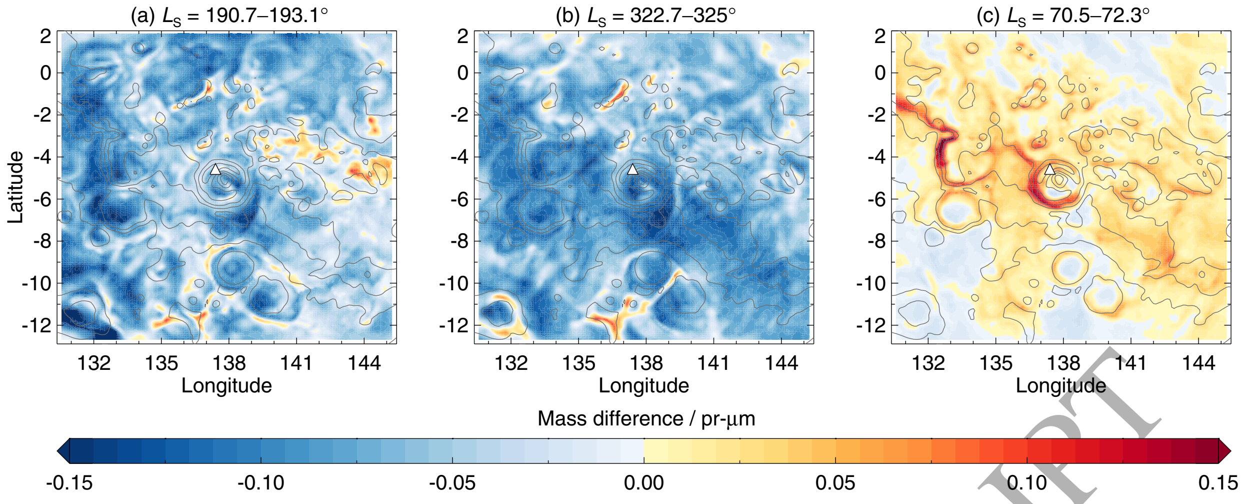

Figure 20: Change in the total subsurface water mass (in precipitable microns) over the last five sols of each simulation. Results are shown for three different periods. The white triangle shows the location of the Curiosity rover, while grey contours show topography.

5. The water cycle in southern hemisphere late summer

5.1. Atmospheric circulation around Gale crater

By late summer in the southern hemisphere ($L_S = 319.8$–$325.0°$) peak daytime temperatures are around 8–10 K lower than at $L_S = 187.8$–$193.1°$, while nighttime temperatures are only around 2 K cooler. Water vapour columns are around half the early spring value. Looking at Figures 13 and 14, it can be seen that there are similarities between the large-scale meridional circulations in early spring and late summer. During the day, the near-surface meridional winds are upslope across the dichotomy boundary (Figure 13a,b), while at night they are downslope (Figure 13d,e), in the opposite direction to the lower branch of the Hadley cell (Figure 14b). As the mean meridional circulation in late summer is stronger than in early spring due to the dustier atmosphere (Figure 14a,b), the nighttime regional downslope winds are weaker.

Figure 22 shows the temperature and wind in the lowest model layer at six different times of day at $L_S = 321°$. Compared with early spring (Figure 12) there are many similarities in the near-surface circulation. By the afternoon, winds around Gale crater are blowing in a southerly direction, with upslope flows along the crater walls being stronger to the south of the crater (Figure 22a). On the north west walls of the crater, the upslope flows meet the north-westerly wind, resulting in a convergence boundary. As night approaches, downslope flows develop, which are initially strongest on the northern crater wall (Figure 22b). As the nighttime wind down the dichotomy boundary is weaker than in early spring, the downslope crater wall winds are also weaker (Figure 22c–d). This is particularly noticeable at 08:00, where downslope winds continue on the southern crater wall in early spring (Figure 12e), but in late summer upslope flows are beginning to develop (Figure 22e). The near-surface

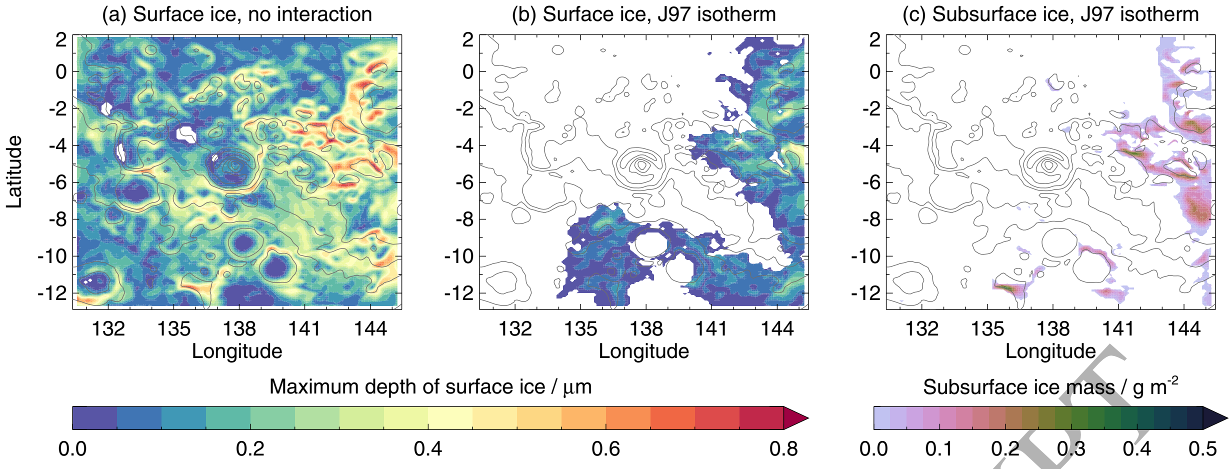

Figure 21: (a) Maximum depth of surface ice over the course of one sol from a simulation without regolith-atmosphere interaction. (b,c) Maximum depth of surface ice and maximum mass of subsurface ice over the course of one sol from a simulation with regolith-atmosphere interaction using the J97 adsorption isotherm. Results are shown for $L_S = 189°$. Black contours show topography, and white shading shows locations where no surface or subsurface ice forms at any time of day.

circulation at $L_S = 321°$ is in broad agreement to that at $L_S = 0°$ in the work of Rafkin et al. (2016). As the circulation patterns are similar in early spring and late summer, the diurnal variation of water in and around Gale crater is similar. As such, here we look more briefly at the water cycle in late summer.

5.2. Comparison with REMS measurements

Figure 23 shows a comparison of RH and water vapour vmr between REMS measurements and the model output. The corresponding temperature and pressure comparisons are shown in Figure 7d–f, where it can be seen that there is generally good agreement between the model and REMS data. As in early spring, the simulation with no regolith-atmosphere interaction appears too wet between around 00:00–09:00 (Figure 23a). Also, the vmr values do not show the same diurnal variation as the REMS measurements (Figure 23b), remaining fairly constant throughout the day, except for decay to ground frost between 04:00–06:00, and a morning peak related to surface ice sublimation. A better agreement with the REMS measurements is achieved when including the regolith diffusion model, with the J97 isotherm again providing the best match in RH between 06:00–10:00. As was the case for early spring, there is general agreement in the 00:00–06:00 vmr values between REMS measurements and model output, but from 18:00–00:00 the model's vmr values are too low. As noted earlier, this could be due to the near-surface being wetter in reality than in the model, or the REMS values could be too high, due to the large uncertainties at this time.

5.3. The water cycle around Gale crater with regolith-atmosphere interaction

Figure 24 shows latitude-altitude (panels a–d) and longitude-altitude (panels e–h) cross sections passing through the location of the Curiosity rover, showing the vapour distribution

ACCEPTED MANUSCRIPT

ACCEPTED MANUSCRIPT

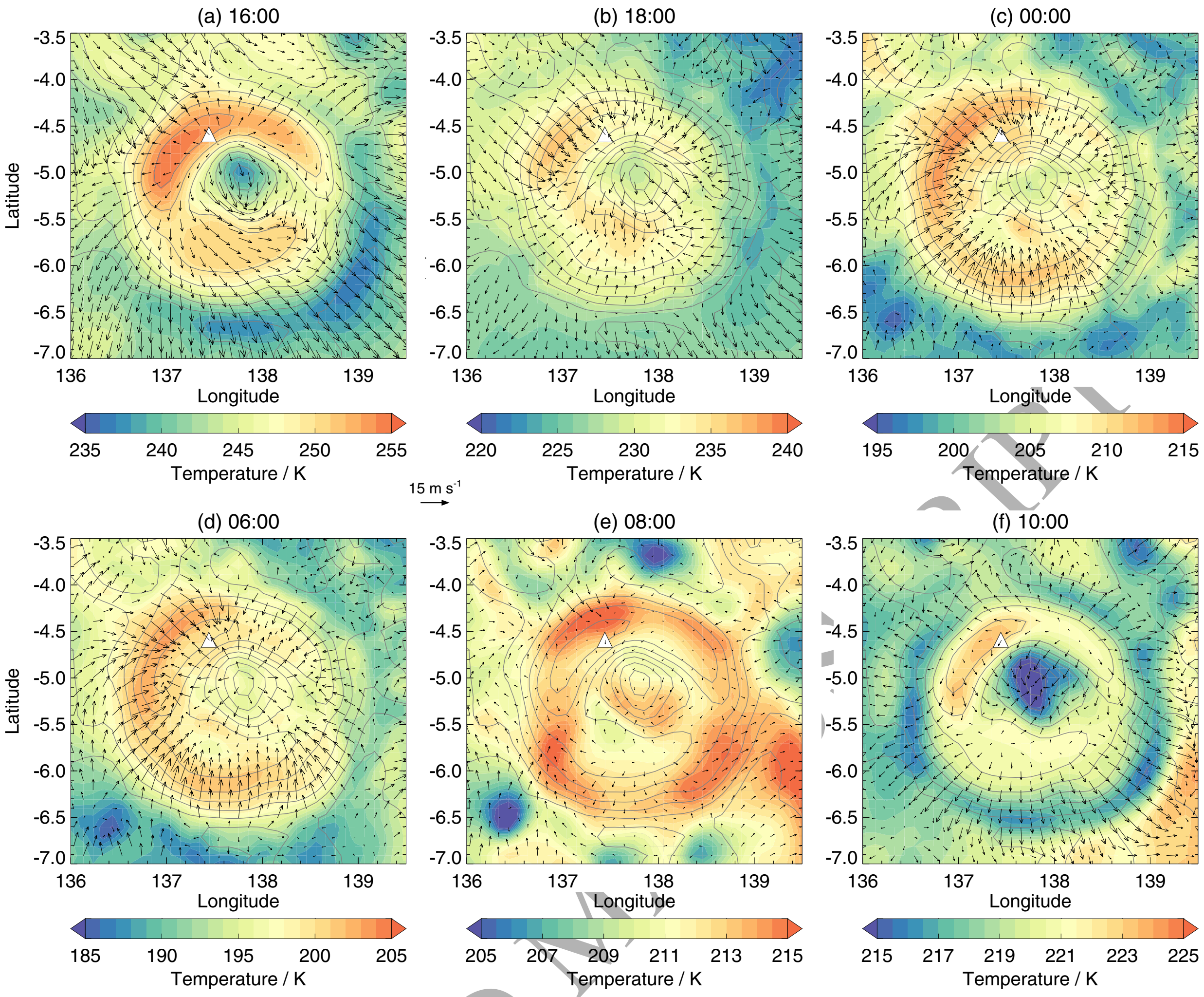

Figure 22: As Figure 12, but for $L_S = 321°$.

from the simulation using the J97 isotherm. As before, the vapour distribution varies on different sols, but the behaviour shown in Figure 24 is representative of this period. At 16:00 (Figure 24a,e), the distribution is similar in the simulations with and without the regolith diffusion model, though the simulation using the J97 isotherm has larger near-surface vapour abundances around the rim of Gale crater due to diffusion from the regolith. By midnight (Figure 24b,f) downslope flows have developed widely. These are strongest on the southern wall of the crater, and hence diffusion into the regolith is largest here, with a peak rate of around 1.5 pr-μm sol^{-1} (Figure 25a). This rate is less than in early spring (see Figure 16a), as the atmospheric vapour abundance is lower.

By 06:00 the large-scale flow across the dichotomy boundary has changed direction, and is now flowing downslope, from south to north (Figure 13e). However, this flow is weaker than in early spring (compare Figure 12d and Figure 22d), and hence the downslope flow on the southern crater wall is not as enhanced (Figure 24c). As such, the flux of vapour into the regolith on the southern crater wall is less than it was at midnight (Figure 25b) whereas

ACCEPTED MANUSCRIPT

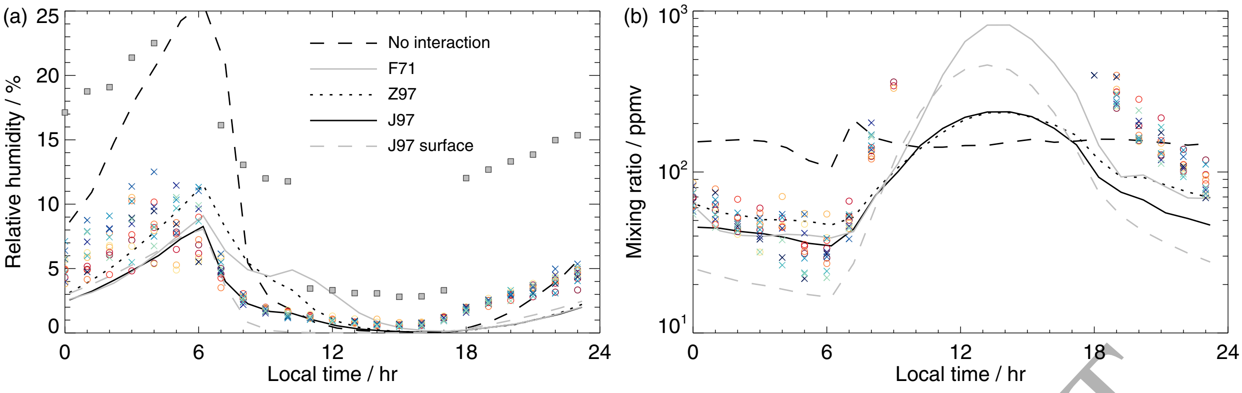

Figure 23: As Figure 9, but for $L_S = 319.8$–$322.7°$.

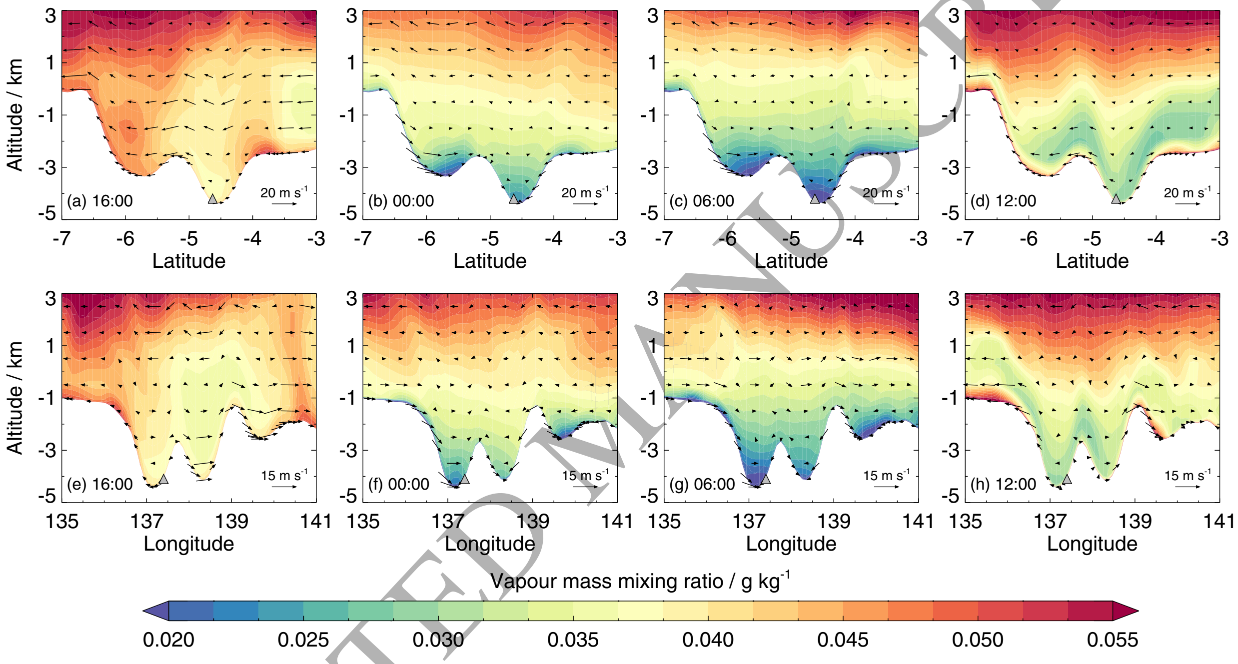

Figure 24: As Figure 15, but for $L_S = 321°$.

in early spring it is larger (Figure 16b). Although the flux is reduced, little of the vapour in the downslope flows reaches the crater floor. In the near-surface layer at the location of the Curiosity rover (at a height of ~2.7 m), the vapour mass mixing ratio is around 3 times smaller than when ignoring regolith-atmosphere interaction, with a value of ~13 mg kg^{-1} (32 ppmv) compared to ~41 mg kg^{-1} (100 ppmv).

Vapour continues to diffuse into the regolith until around 09:00, when the rapidly-warming atmosphere and subsurface results in a large flux of vapour out of the regolith (due to desorption of vapour from the regolith grains). As in early spring, this flux is strongest on the southern and eastern crater walls as the strong upslope winds transport the vapour away, allowing more to diffuse out of the regolith. By midday the flux out of the regolith in these regions is around 2.5–3 pr-μm sol^{-1} (Figure 25c). This is lower than

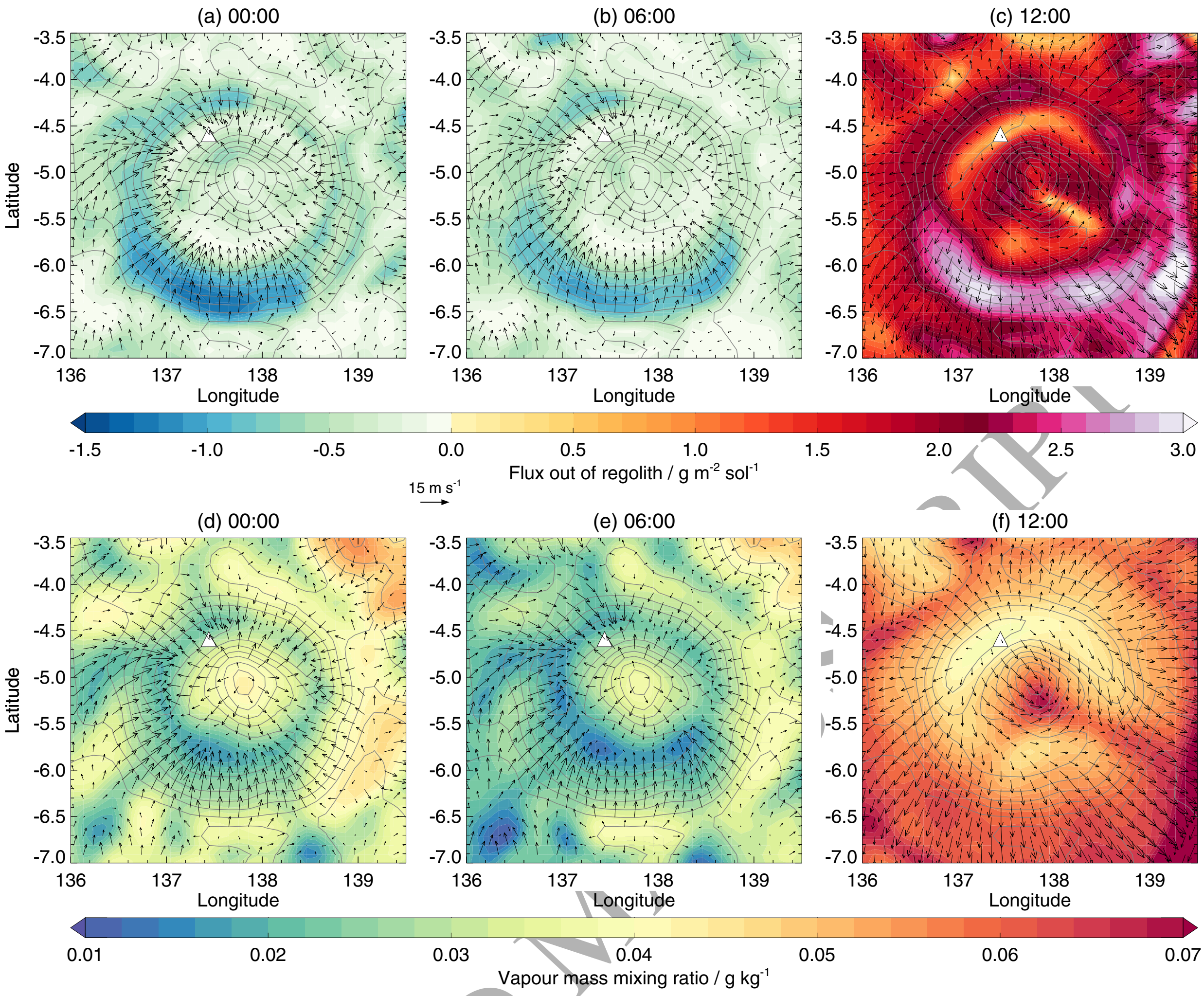

Figure 25: As Figure 16, but for $L_S = 321°$.

ACCEPTED MANUSCRIPT

in early spring, as the flux into the regolith during the night was lower. Again, the flux out of the regolith results in a three-layer structure in the vapour distribution (Figure 24d,h) with relatively large vapour values in the lowest few hundred metres, a drier layer around 1–2 km deep above, and then increased vapour amounts above. When regolith interaction is not taken into account, there is only a two-layer structure present, as the large near-surface vapour abundances are not present. Additionally, the dry layer is less dry when ignoring regolith interaction, as the air within the crater at night has a larger vapour abundance.

Unlike early spring, there is little cloud cover in the mesoscale domain during late summer due to the warmer atmospheric temperatures. Surface ice is also reduced in terms of both spatial coverage, and depth. When ignoring regolith interaction, peak nighttime ice depths to the east of Gale crater are around 0.3 μm, compared to 0.8 μm in early spring. Inclusion of regolith interaction causes a large reduction in surface ice formation, as it did in early spring, with ice only present to the north and east of Gale crater, with thicknesses of around 0.1 μm. Subsurface ice is almost non-existent, with only a couple of patches of ice in the

ACCEPTED MANUSCRIPT

upper few millimetres of regolith to the east of Gale crater.

In terms of the overall loss or gain of subsurface water, Figure 20b shows the change in the total subsurface water content over the last five sols of the simulation with the J97 isotherm. The results are similar to the early spring case, where in general mass is being lost from the subsurface, though certain locations on topographic slopes are gaining mass. As noted earlier, this is because the initial regolith water distribution came from GCM output, which cannot account for the small-scale circulation patterns and temperature variations resolved by the mesoscale model.

6. The water cycle during aphelion

6.1. Atmospheric circulation around Gale crater

Finally we look at the water cycle around aphelion season ($L_S = 68.3$–$72.3°$). Compared to late summer, temperatures are around 15–20 K lower, and water vapour column values have roughly halved. The meridional circulation around aphelion is different to the two periods considered previously. There are still upslope winds across the dichotomy boundary during the day, and downslope winds at night (Figure 13c,d), but now the lower branch of the Hadley cell is transporting air downslope across the dichotomy boundary (Figure 14c). As such, the upslope daytime flow is weaker, and downslope nighttime flow is stronger, than in the previous two periods.

Figure 26 shows the temperature and wind in the lowest model layer at six different times of day at $L_S = 69°$. The near-surface circulation resembles that in early spring (Figure 12) more closely than that in late summer (Figure 22) due to the stronger nighttime downslope flows across the dichotomy boundary. This results in strong downslope winds on the southern and western crater walls from 21:00–08:00 (Figure 26c–e). During the afternoon, the weaker upslope flows across the dichotomy boundary result in weaker upslope flows on the southern wall of the crater (Figure 26a,f) compared to the other periods. The near-surface circulation at $L_S = 69°$ is in broad agreement to that at $L_S = 90°$ in the work of Rafkin et al. (2016).

6.2. Comparison with REMS measurements

Figure 27 shows a comparison of RH and water vapour vmr between REMS measurements and the model output. The corresponding temperature and pressure comparisons are shown in Figure 7g–i. At this time, peak RH values are ∼35%, which is larger than in the two periods considered previously (∼15% in early spring and ∼10% in late summer). During the early morning (00:00–06:00) all of the simulations produce RH and vmr results comparable to the REMS measurements, even the simulation with no regolith-atmosphere interaction. REMS measurements suggest that surface frost could have formed during this period (Martínez et al., 2015), as it did in the simulation with no regolith-atmosphere interaction. However, diffusion of vapour into the regolith is required to avoid the RH ‘jump’ seen at 08:00 in the simulation without regolith-atmosphere interaction, which is caused by

ACCEPTED MANUSCRIPT

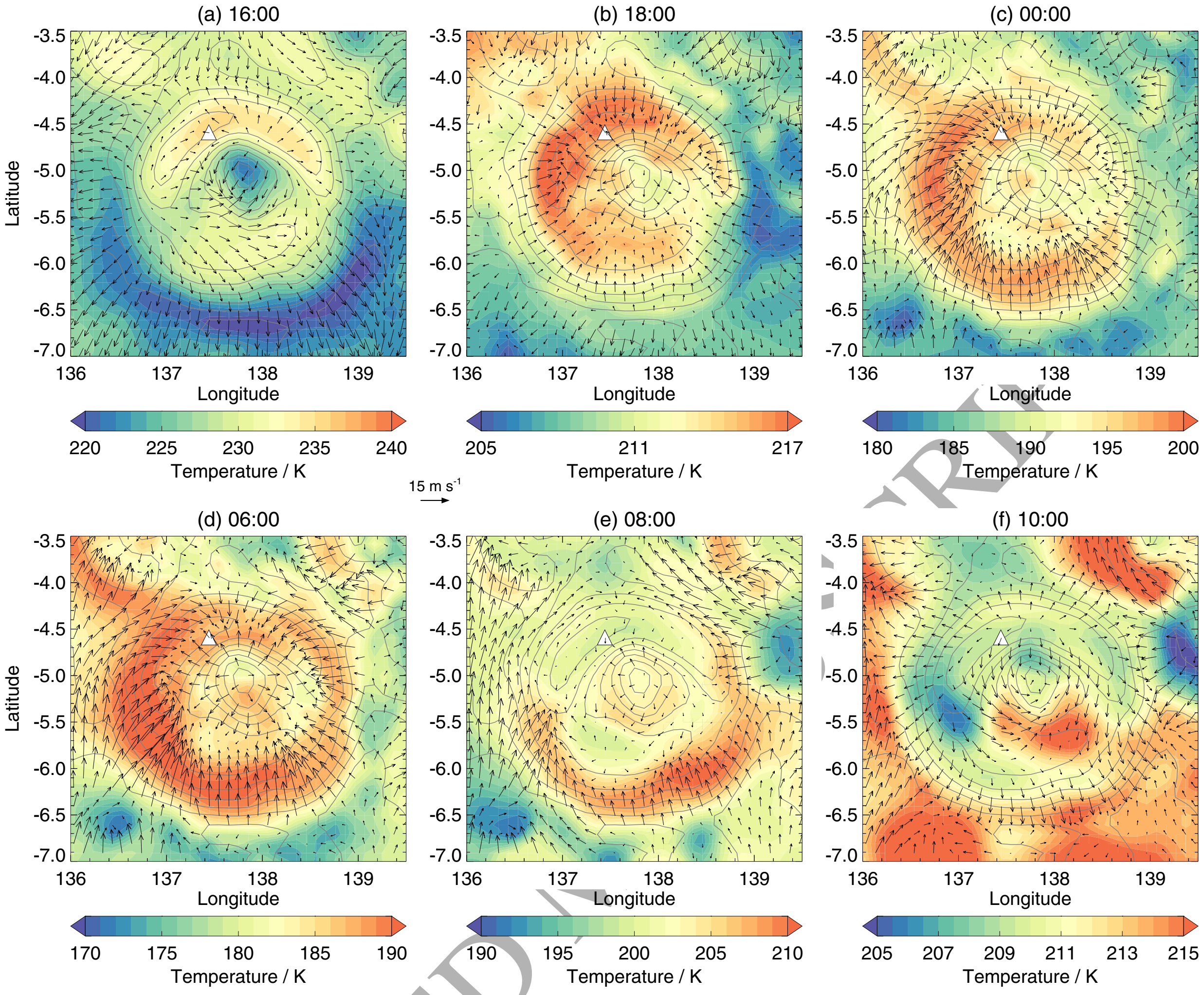

Figure 26: As Figure 12, but for $L_S = 69°$.

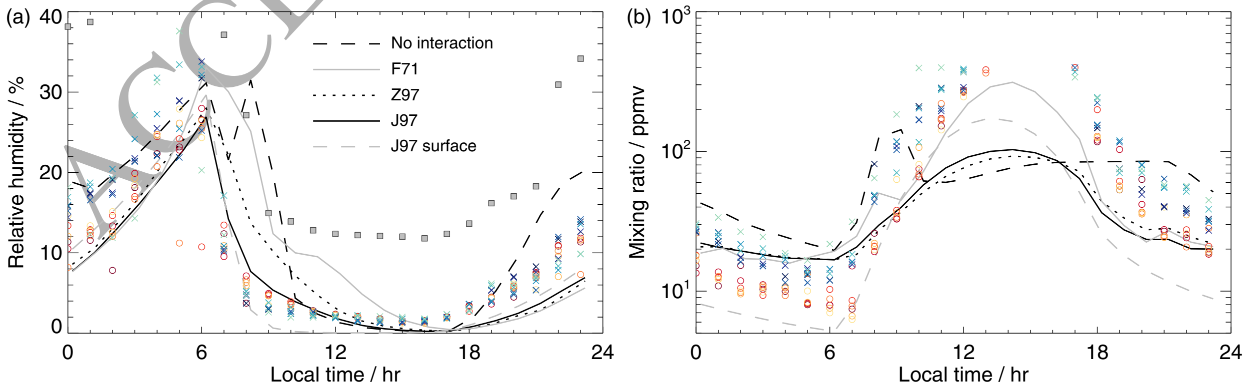

Figure 27: As Figure 9, but for $L_S = 68.3$–$70.5°$.

ACCEPTED MANUSCRIPT

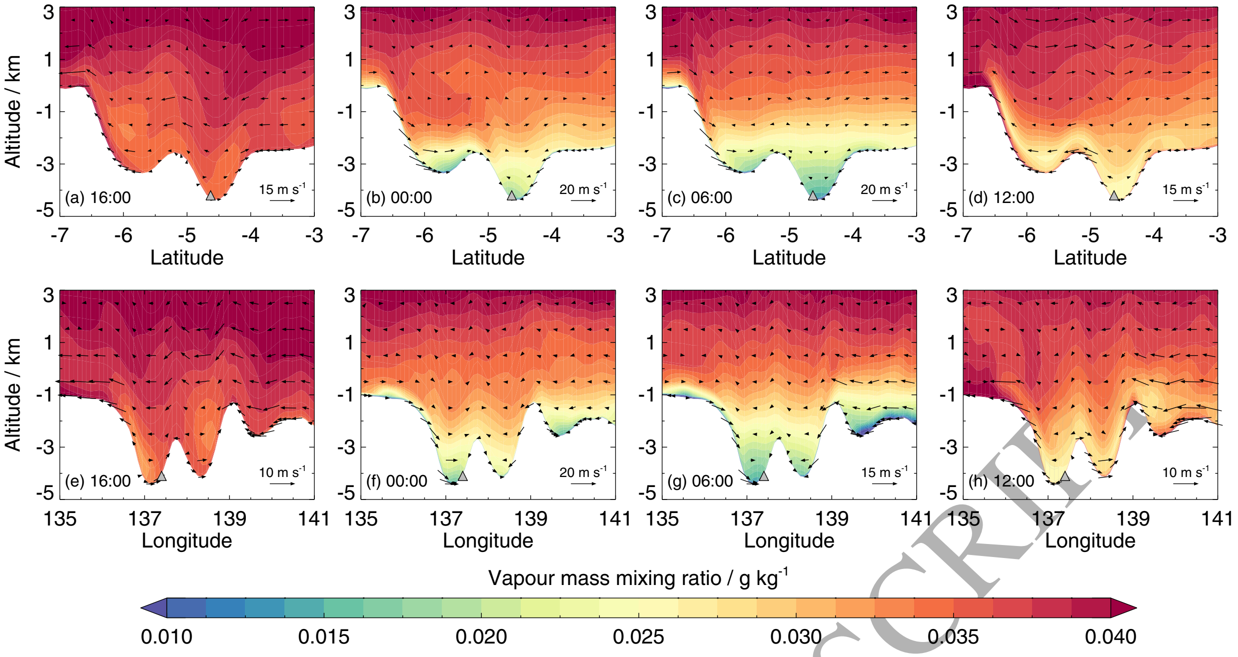

Figure 28: As Figure 15, but for $L_S = 69°$.

the sublimation of surface ice. The J97 isotherm provides the best match to the decreasing RH between 06:00–12:00. Between 18:00–00:00, the simulations with regolith interaction show an increase in RH comparable to the REMS data, though the RH values are around 4% too low (and the vmr values are thus also too low). This behaviour is similar to that seen in the previous two periods, and could be due to the near-surface atmosphere in the model being too dry in the late evening, or the REMS measurements being larger than reality.

6.3. The water cycle around Gale crater with regolith-atmosphere interaction

Figure 28 shows latitude-altitude (panels a–d) and longitude-altitude (panels e–h) cross sections passing through the location of the Curiosity rover, showing the vapour distribution from the simulation using the J97 isotherm. Unlike the previous two periods (early spring and late summer) the vapour distributions are similar in the simulations with and without regolith interaction. This is due to the lower temperatures at this time of year. At night, the cold temperatures result in widespread ice formation (see Figure 29), which reduces the near-surface vapour values and hence reduces the flux of vapour into the regolith. During the day, peak temperatures are around 25–35 K lower than in the other two periods, which results in less diffusion of vapour from the regolith, as less vapour is desorbed from the regolith grains.

At 16:00 (Figure 28a,e) vapour is generally well mixed in the atmosphere. By midnight (Figure 28b,f) downslope flows have developed widely. These are strongest on the southern wall of the crater, and hence diffusion into the regolith is largest here, with a peak rate of around 1 pr-μm sol^{-1} (Figure 30a). In the simulation with no regolith-atmosphere interac-

ACCEPTED MANUSCRIPT

ACCEPTED MANUSCRIPT

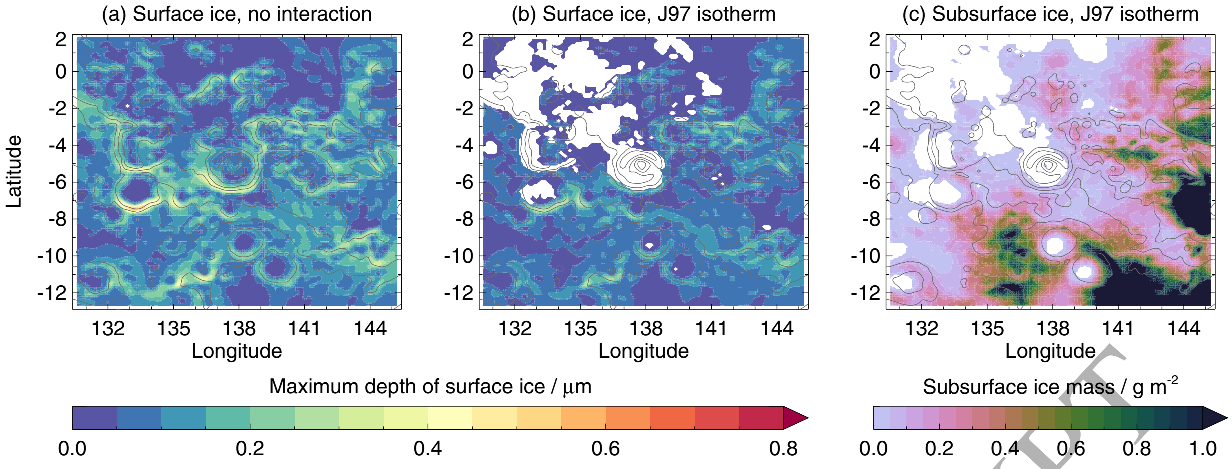

Figure 29: As Figure 21, but for $L_S = 69°$.

tion, similar behaviour as in Figure 28b,f is seen, but the reduction in near-surface vapour is caused by ice formation on the surface, rather than diffusion into the regolith. By 06:00, extensive surface ice has formed in all simulations. When regolith-atmosphere interaction is ignored, surface ice forms everywhere (Figure 29a), which results in depleted near-surface vapour values. When including the regolith diffusion model, no surface ice forms on the floor of Gale crater (Figure 29b), and the low vapour values here are due to diffusion into the regolith and adsorption onto regolith grains. The thickness of the surface ice is a few tenths of a micron, which is in agreement with the values determined from REMS measurements (Martínez et al., 2015).

Once surface ice has formed, diffusion into the regolith is stopped (Figure 30b). Thus, the subsurface ice deposits which form (Figure 29c) do so between around 22:00–06:00. This subsurface ice rapidly disappears at around 07:00, as temperatures begin to rise. By midday, upslope flows have developed on the walls of Gale crater, with the strongest winds on the southern crater wall. The flux out of the regolith in these regions is around 1.5–2 pr-μm sol^{-1} (Figure 30c). This results in a three-layer structure in the vapour distribution (Figure 28d,h), though not as pronounced as in the other seasons (as less vapour diffused into the regolith during the night). A three-layer structure is also seen in the simulation without regolith interaction, with large near-surface vapour abundances caused by the surface ice deposits subliming.

At $L_S = 69°$, cloud cover is much more extensive than at $L_S = 189°$ due to the colder temperatures, with clouds present at all times of day. The cloud formations have slight variations depending on the sol, but those shown in Figure 31 are representative of the general behaviour. Peak optical depths occur between 21:00 and midnight depending on the sol, with the infrared absorption-only optical depths varying between 0.1–0.15. As was the case at $L_S = 189°$, the optical thickness of the clouds is not large enough to lead to any appreciable daytime cooling of the surface. The clouds generally have a greater vertical

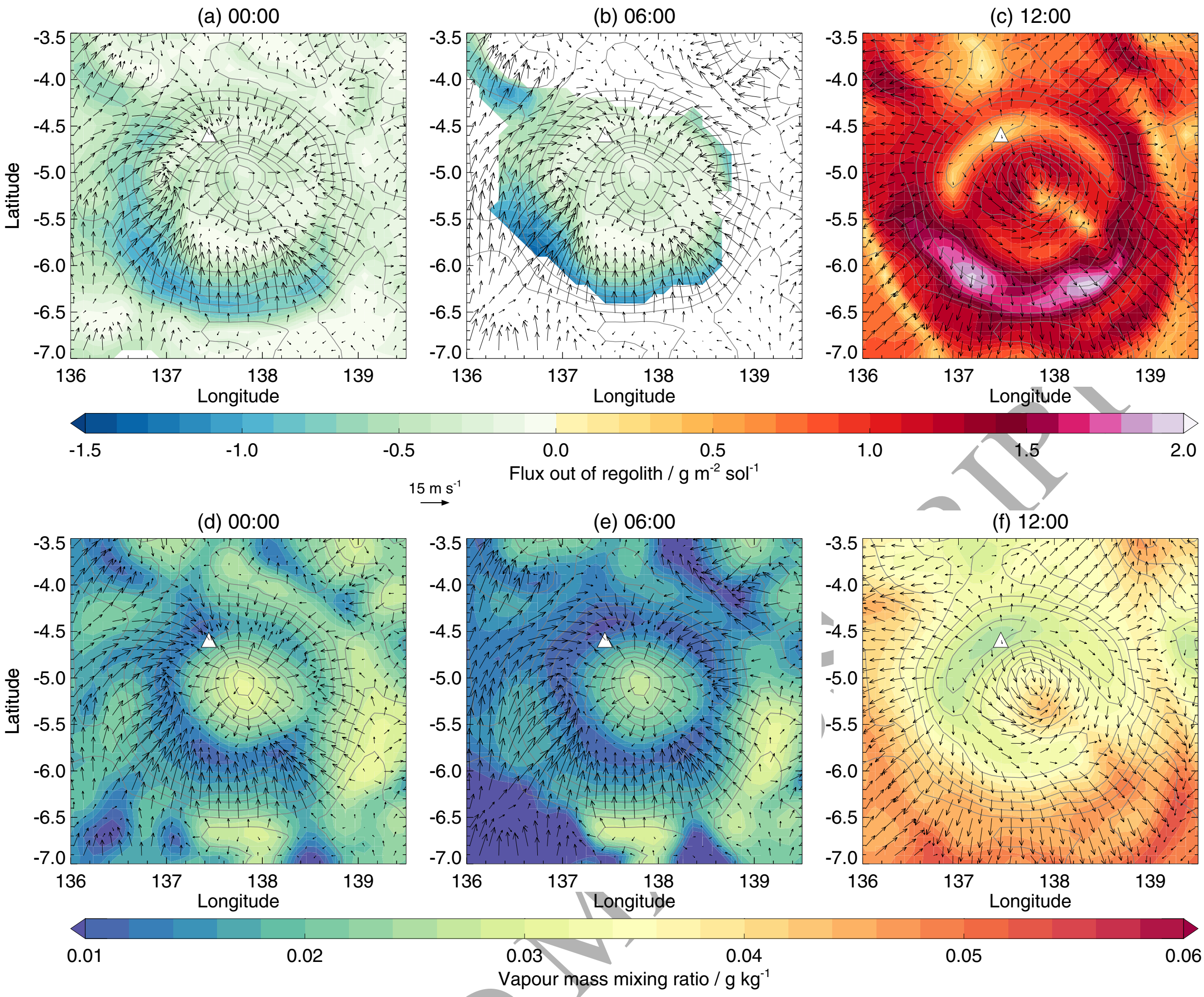

Figure 30: As Figure 16, but for $L_S = 69°$.

extent than those at $L_S = 189°$. In the late evening and early morning, a two-layer structure is seen, with one cloud layer between 10–25 km, and another with a base at around 30 km. (Figure 31a,e). Near-surface 'fogs' also form in the early morning in locations to the south and east of Gale crater, with ice particles ~5–8 μm in size. As the morning progresses the cloud splits into three layers, with a thicker cloud at around 10 km, and thinner clouds above at around 20 km and 30 km (Figure 31c,g). By late afternoon, the lower cloud layer has been affected by wave activity associated with the topography around Gale crater (Figure 31d,h). As evening progresses, the cloud layers thicken again, and resemble those in Figure 31a,e. The peak opacities of the clouds (infrared extinction opacities per kilometre) range from $10^{-1.5}$ at 10 km to $10^{-4.5}$ at 40 km. These opacities are potentially large enough for heating of ~8 K sol^{-1} during the day, and cooling of ~2–4 K sol^{-1} at night both at and above cloud-forming height (Steele et al., 2014a). The heating rates are lower than at $L_S = 189°$, as the thickest clouds form lower in the atmosphere where the density is larger.

In terms of the loss or gain of subsurface water, Figure 20c shows the change in the total

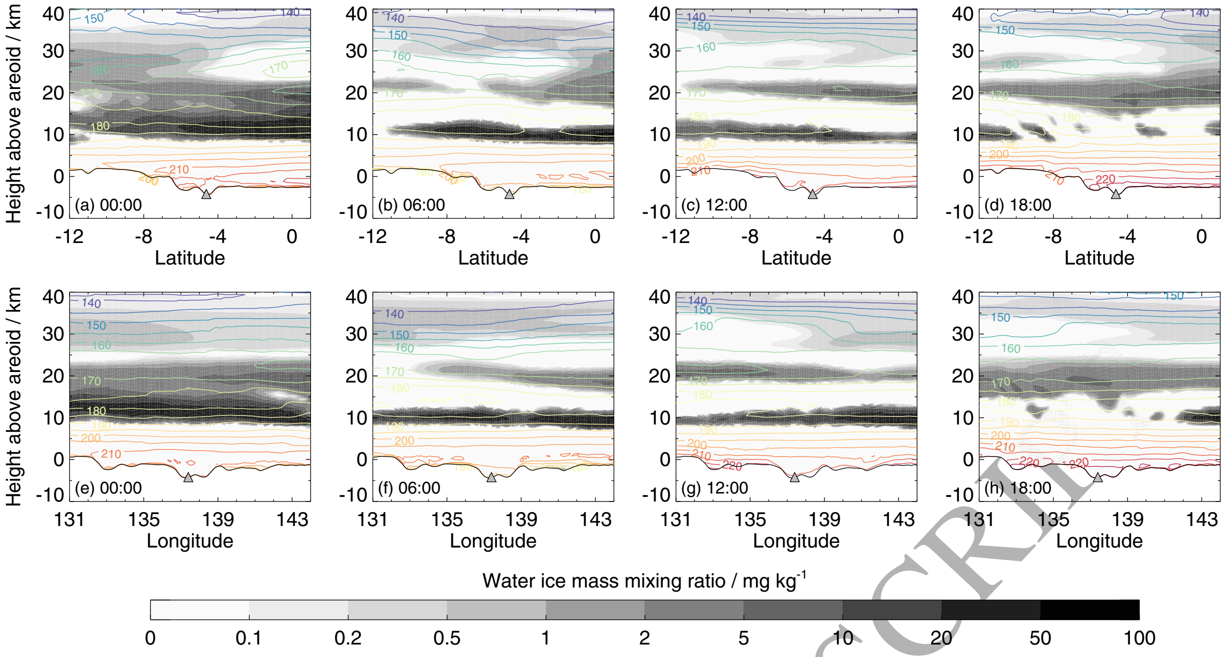

Figure 31: As Figure 17, but for $L_S = 69°$.

subsurface water content over the last five sols of the simulation with the J97 isotherm. Unlike the early spring and late summer cases, where in general mass is being lost from the subsurface, there are large areas where the subsurface water mass is increasing, which is particularly noticeable on crater walls. This mass corresponds to increases in adsorbed water at depths of 2–3 cm, where peak temperatures, which range from 230–240 K, are not large enough to cause a loss of water to the surface through desorption. Away from the crater walls, the mass gain/loss is typically around 0.025 pr-μm, which is 200 times smaller than the typical atmospheric water vapour column values at this time.

7. Conclusions

We have performed mesoscale simulations of the water cycle in a region around Gale crater, both with and without regolith-atmosphere interaction. While not covering exactly the same periods, the near surface circulations in our simulations around $L_S = 189°$, $L_S = 321°$ and $L_S = 69°$ are in broad agreement with those of Rafkin et al. (2016) at $L_S = 180°$, $L_S = 0°$ and $L_S = 90°$ respectively, and that of Tyler and Barnes (2013) at $L_S = 151°$. When comparing our results with measurements from the REMS instrument on board the Curiosity rover, there is good agreement in terms of pressure and temperature, while the broad wind patterns are also captured. In terms of the water cycle, it is clear that diffusion of vapour in and out of the regolith, and adsorption/desorption onto regolith grains, needs to be taken into account in order to match the diurnal variation in relative humidity, as was the case in the 1D simulations of Savijärvi et al. (2016). When ignoring regolith interaction, the water vapour volume mixing ratio displays a decline after midnight with a morning

ACCEPTED MANUSCRIPT

ACCEPTED MANUSCRIPT

peak, but is then fairly constant for the remainder of the day. This is due to the formation and sublimation of surface ice, and is similar to the behaviour seen in some Phoenix TECP measurements (Zent et al., 2016). The best agreement between the model and REMS occurs when using the adsorption isotherm from Jakosky et al. (1997).

In all of the three periods considered (covering southern hemisphere early spring, late summer and around aphelion) vapour is generally well mixed within Gale crater by late afternoon. Throughout the evening and night, flows down the crater walls and down Mount Sharp transport vapour into the crater. When including regolith-atmosphere interaction, the amount of vapour reaching the crater floor is reduced due to the diffusion of vapour along the crater walls, where it becomes adsorbed onto regolith grains. At the location of the Curiosity rover, the inclusion of regolith-atmosphere interaction reduces the nighttime vapour mass mixing ratios by factors of 2 and 3 during southern hemisphere early spring and late summer respectively. Around aphelion, nighttime vapour values at the location of the Curiosity rover are similar in simulations with and without regolith interaction. In the simulations without regolith interaction, the reduction of near-surface vapour at night is caused by the formation of surface ice, rather than diffusion into the regolith.

The transport of vapour into Gale crater is affected by the atmospheric flow over the dichotomy boundary. In the evening the regional wind blows up the dichotomy boundary (from north to south), and as the northern wall of Gale crater slopes downwards in the direction of this wind, the downslope winds are initially stronger on the northern crater walls. These winds transport vapour from above the rim of Gale crater, and hence the flux of water into the regolith is initially largest on the northern crater wall. By early morning the direction of the dichotomy boundary flow has reversed, and now the southern wall of Gale crater slopes downwards in the direction of the wind, leading to larger fluxes of water into the regolith here. As Curiosity is located at the base of Mount Sharp it is affected by the nighttime downslope flow, but this flow is relatively weak, and vapour abundances above Mount Sharp are relatively low. As such, the vapour abundance at the Curiosity rover location is only a few percent larger than that a few kilometres north at the lowest point of the crater floor. (This difference increases to $\sim$20% at 40 m above the surface.)

During the morning and afternoon, desorbed vapour diffuses out of the regolith and is transported in winds up the crater walls. As the dichotomy boundary flow travels from north to south, winds are strongest towards the southern rim of the crater. These winds advect the diffusing vapour up the crater walls, allowing more vapour to be released from the subsurface and hence leading to larger fluxes here. The vapour at the crater rims can be transported a few hundred metres into the air at the locations of convergence boundaries, where it is eventually advected by the large-scale wind. However, as the regions of large vapour abundance at the crater rim are accompanied by regions of relatively low vapour abundance in a layer above (from the transport of dry air from within the crater) these features are almost undetectable when looking at the column vapour abundance. While the

ACCEPTED MANUSCRIPT

discussion above has focused on Gale crater, similar phenomena appear at the majority of craters resolvable in the mesoscale domain.

Regolith-atmosphere interaction limits the formation of surface ice in the Gale crater latitudes by reducing the nighttime vapour amounts in the lower atmosphere. In southern hemisphere early spring and late summer no surface ice forms on the floors of craters, though ice still forms in the early morning (between 05:00–07:00) on eastern crater walls (particularly in the Lasswitz and Wien craters) as these are ∼10 K colder at this time than the western crater walls. Surface ice is much more abundant around aphelion. At this time, the REMS relative humidity measurements between 00:00–06:00 can be matched by simulations with and without a regolith diffusion model. In the latter case, it is the formation of surface ice on the crater floor that reduces the near-surface vapour abundance, as opposed to adsorption and diffusion of vapour into the regolith.

REMS measurements suggest that surface frost could only have formed between sols 400–710 of the first 1000 sols of the mission (Martínez et al., 2015). During this time, the estimated thermal inertias of the ground were ∼200 tiu. In the mesoscale model, the thermal inertias are larger at ∼290 tiu. In the simulations with regolith-atmosphere interaction, this larger thermal inertia value limits the formation of surface ice due to the resulting warmer model nighttime ground temperatures. However, the simulations around aphelion (corresponding to MSL sols 496–501) do show much more extensive surface ice, so a reduction in the thermal inertia in the mesoscale model would likely lead to frost formation on the floor of Gale crater, as suggested by the REMS measurements. Subsurface ice is sparsely distributed in southern hemisphere early spring and late summer, but is more extensive around aphelion. However, the ice amounts are small, only exist in the upper few millimetres of regolith, and completely sublime during the day.

Acknowledgements

This work was funded by the UK Science and Technology Facilities Council, grant number ST/L000776/1. The authors thank Scot Rafkin and an anonymous reviewer, whose comments helped improve this paper.

References

Aharonson, O., Schorghofer, N., 2006. Subsurface ice on Mars with rough topography. J. Geophys. Res. (Planets) 111, E11007.

Böttger, H. M., Lewis, S. R., Read, P. L., Forget, F., 2004. The effect of a global dust storm on simulations of the Martian water cycle. Geophys. Res. Lett. 31, L22702.

Böttger, H. M., Lewis, S. R., Read, P. L., Forget, F., 2005. The effects of the martian regolith on GCM water cycle simulations. Icarus 177, 174–189.

Boynton, W. V., Feldman, W. C., Squyres, S. W., Prettyman, T. H., Brückner, J., Evans, L. G., Reedy, R. C., Starr, R., Arnold, J. R., Drake, D. M., Englert, P. A. J., Metzger, A. E., Mitrofanov, I., Trombka, J. I., d'Uston, C., Wänke, H., Gasnault, O., Hamara, D. K., Janes, D. M., Marcialis, R. L., Maurice, S.,

ACCEPTED MANUSCRIPT

Mikheeva, I., Taylor, G. J., Tokar, R., Shinohara, C., 2002. Distribution of Hydrogen in the Near Surface of Mars: Evidence for Subsurface Ice Deposits. Science 297, 81–85.

Chamberlain, M. A., Boynton, W. V., 2007. Response of Martian ground ice to orbit-induced climate change. J. Geophys. Res. (Planets) 112.

Clancy, R. T., Wolff, M. J., Christensen, P. R., 2003. Mars aerosol studies with the MGS TES emission phase function observations: Optical depths, particle sizes, and ice cloud types versus latitude and solar longitude. J. Geophys. Res. (Planets) 108, 5098.

Fanale, F. P., Cannon, W. A., 1971. Adsorption on the Martian Regolith. Nature 230, 502–504.

Fanale, F. P., Jakosky, B. M., 1982. Regolith-atmosphere exchange of water and carbon dioxide on Mars - Effects on atmospheric history and climate change. Planet. Space Sci. 30, 819–831.

Farmer, C. B., Davies, D. W., Holland, A. L., Laporte, D. D., Doms, P. E., 1977. Mars - Water vapor observations from the Viking orbiters. J. Geophys. Res. 82, 4225–4248.

Feldman, W. C., Prettyman, T. H., Maurice, S., Plaut, J. J., Bish, D. L., Vaniman, D. T., Mellon, M. T., Metzger, A. E., Squyres, S. W., Karunatillake, S., Boynton, W. V., Elphic, R. C., Funsten, H. O., Lawrence, D. J., Tokar, R. L., 2004. Global distribution of near-surface hydrogen on Mars. J. Geophys. Res. (Planets) 109.

Forget, F., Hourdin, F., Fournier, R., Hourdin, C., Talagrand, O., Collins, M., Lewis, S. R., Read, P. L., Huot, J.-P., 1999. Improved general circulation models of the Martian atmosphere from the surface to above 80 km. J. Geophys. Res. 104, 24155–24176.

Glenar, D. A., Samuelson, R. E., Pearl, J. C., Bjoraker, G. L., Blaney, D., 2003. Spectral imaging of martian water ice clouds and their diurnal behavior during the 1999 aphelion season ($L_s = 130°$). Icarus 161, 297–318.

Gómez-Elvira, J., Armiens, C., Carrasco, I., Genzer, M., Gómez, F., Haberle, R., Hamilton, V. E., Harri, A.-M., Kahanpää, H., Kemppinen, O., Lepinette, A., Martín Soler, J., Martín-Torres, J., Martínez-Frías, J., Mischna, M., Mora, L., Navarro, S., Newman, C., Pablo, M. A., Peinado, V., Polkko, J., Rafkin, S. C. R., Ramos, M., Rennó, N. O., Richardson, M., Rodríguez-Manfredi, J. A., Romeral Planelló, J. J., Sebastián, E., Torre Juárez, M., Torres, J., Urquí, R., Vasavada, A. R., Verdasca, J., Zorzano, M.-P., 2014. Curiosity's rover environmental monitoring station: Overview of the first 100 sols. J. Geophys. Res. (Planets) 119, 1680–1688.

Gómez-Elvira, J., Armiens, C., Castañer, L., Domínguez, M., Genzer, M., Gómez, F., Haberle, R., Harri, A.-M., Jiménez, V., Kahanpää, H., Kowalski, L., Lepinette, A., Martín, J., Martínez-Frías, J., McEwan, I., Mora, L., Moreno, J., Navarro, S., de Pablo, M. A., Peinado, V., Peña, A., Polkko, J., Ramos, M., Renno, N. O., Ricart, J., Richardson, M., Rodríguez-Manfredi, J., Romeral, J., Sebastián, E., Serrano, J., de la Torre Juárez, M., Torres, J., Torrero, F., Urquí, R., Vázquez, L., Velasco, T., Verdasca, J., Zorzano, M.-P., Martín-Torres, J., 2012. REMS: The Environmental Sensor Suite for the Mars Science Laboratory Rover. Space Sci. Rev. 170, 583–640.

Guzewich, S. D., Newman, C. E., de la Torre Juárez, M., Wilson, R. J., Lemmon, M., Smith, M. D., Kahanpää, H., Harri, A.-M., 2016. Atmospheric tides in Gale Crater, Mars. Icarus 268, 37–49.

Haberle, R. M., Gómez-Elvira, J., Torre Juárez, M., Harri, A.-M., Hollingsworth, J. L., Kahanpää, H., Kahre, M. A., Lemmon, M., Martín-Torres, F. J., Mischna, M., Moores, J. E., Newman, C., Rafkin, S. C. R., Rennó, N., Richardson, M. I., Rodríguez-Manfredi, J. A., Vasavada, A. R., Zorzano-Mier, M.-P., 2014. Preliminary interpretation of the REMS pressure data from the first 100 sols of the MSL mission. J. Geophys. Res. (Planets) 119, 440–453.

Harri, A.-M., Genzer, M., Kemppinen, O., Gomez-Elvira, J., Haberle, R., Polkko, J., Savijärvi, H., Rennó, N., Rodriguez-Manfredi, J. A., Schmidt, W., Richardson, M., Siili, T., Paton, M., Torre-Juarez, M. D. L., Mäkinen, T., Newman, C., Rafkin, S., Mischna, M., Merikallio, S., Haukka, H., Martin-Torres, J., Komu, M., Zorzano, M.-P., Peinado, V., Vazquez, L., Urqui, R., 2014a. Mars Science Laboratory relative humidity observations: Initial results. J. Geophys. Res. (Planets) 119, 2132–2147.

Harri, A.-M., Genzer, M., Kemppinen, O., Kahanpää, H., Gomez-Elvira, J., Rodriguez-Manfredi, J. A., Haberle, R., Polkko, J., Schmidt, W., Savijärvi, H., Kauhanen, J., Atlaskin, E., Richardson, M., Siili, T., Paton, M., Torre Juarez, M., Newman, C., Rafkin, S., Lemmon, M. T., Mischna, M., Merikallio, S., Haukka, H., Martin-Torres, J., Zorzano, M.-P., Peinado, V., Urqui, R., Lapinette, A., Scodary, A., Mäkinen, T., Vazquez, L., Rennó, N., REMS/MSL Science Team, 2014b. Pressure observations by the Curiosity rover: Initial results. J. Geophys. Res. (Planets) 119, 82–92.

Jakosky, B. M., Farmer, C. B., 1982. The seasonal and global behavior of water vapor in the Mars atmosphere - Complete global results of the Viking atmospheric water detector experiment. J. Geophys. Res. 87, 2999–3019.

Jakosky, B. M., Zent, A. P., Zurek, R. W., 1997. The Mars Water Cycle: Determining the Role of Exchange with the Regolith. Icarus 130, 87–95.

Lewis, S. R., Collins, M., Read, P. L., Forget, F., Hourdin, F., Fournier, R., Hourdin, C., Talagrand, O., Huot, J.-P., 1999. A climate database for Mars. J. Geophys. Res. 104, 24177–24194.

Lewis, S. R., Read, P. L., Conrath, B. J., Pearl, J. C., Smith, M. D., 2007. Assimilation of thermal emission spectrometer atmospheric data during the Mars Global Surveyor aerobraking period. Icarus 192, 327–347.

Madeleine, J.-B., Forget, F., Spiga, A., Wolff, M. J., Montmessin, F., Vincendon, M., Jouglet, D., Gondet, B., Bibring, J.-P., Langevin, Y., Schmitt, B., 2012. Aphelion water-ice cloud mapping and property retrieval using the OMEGA imaging spectrometer onboard Mars Express. J. Geophys. Res. (Planets) 117.

Maltagliati, L., Montmessin, F., Korablev, O., Fedorova, A., Forget, F., Määttänen, A., Lefèvre, F., Bertaux, J.-L., 2013. Annual survey of water vapor vertical distribution and water-aerosol coupling in the martian atmosphere observed by SPICAM/MEx solar occultations. Icarus 223, 942–962.

Maltagliati, L., Titov, D. V., Encrenaz, T., Melchiorri, R., Forget, F., Keller, H. U., Bibring, J.-P., 2011. Annual survey of water vapor behavior from the OMEGA mapping spectrometer onboard Mars Express. Icarus 213, 480–495.

Martín-Torres, F. J., Zorzano, M.-P., Valentín-Serrano, P., Harri, A.-M., Genzer, M., Kemppinen, O., Rivera-Valentin, E. G., Jun, I., Wray, J., Bo Madsen, M., Goetz, W., McEwen, A. S., Hardgrove, C., Renno, N., Chevrier, V. F., Mischna, M., Navarro-González, R., Martínez-Frías, J., Conrad, P., McConnochie, T., Cockell, C., Berger, G., R. Vasavada, A., Sumner, D., Vaniman, D., 2015. Transient liquid water and water activity at Gale crater on Mars. Nat. Geosci. 8, 357–361.

Martínez, G. M., Fischer, E., Renn, N. O., Sebastin, E., Kemppinen, O., Bridges, N., Borlina, C. S., Meslin, P.-Y., Genzer, M., Harri, A.-H., Vicente-Retortillo, A., Ramos, M., de la Torre Jurez, M., Gmez, F., Gmez-Elvira, J., 2015. Likely frost events at Gale crater: Analysis from MSL/REMS measurements. Icarus.

Martínez, G. M., Rennó, N., Fischer, E., Borlina, C. S., Hallet, B., Torre Juárez, M., Vasavada, A. R., Ramos, M., Hamilton, V., Gomez-Elvira, J., Haberle, R. M., 2014. Surface energy budget and thermal inertia at Gale Crater: Calculations from ground-based measurements. J. Geophys. Res. (Planets) 119, 1822–1838.

Maurice, S., Feldman, W., Diez, B., Gasnault, O., Lawrence, D. J., Pathare, A., Prettyman, T., 2011. Mars Odyssey neutron data: 1. Data processing and models of water-equivalent-hydrogen distribution. J. Geophys. Res.(Planets) 116, 11008.

McCleese, D. J., Heavens, N. G., Schofield, J. T., Abdou, W. A., Bandfield, J. L., Calcutt, S. B., Irwin, P. G. J., Kass, D. M., Kleinböhl, A., Lewis, S. R., Paige, D. A., Read, P. L., Richardson, M. I., Shirley, J. H., Taylor, F. W., Teanby, N., Zurek, R. W., 2010. Structure and dynamics of the Martian lower and middle atmosphere as observed by the Mars Climate Sounder: Seasonal variations in zonal mean temperature, dust, and water ice aerosols. J. Geophys. Res. (Planets) 115, E12016.

ACCEPTED MANUSCRIPT

ACCEPTED MANUSCRIPT

Mellon, M. T., Feldman, W. C., Prettyman, T. H., 2004. The presence and stability of ground ice in the southern hemisphere of Mars. Icarus 169, 324–340.

Mellon, M. T., Jakosky, B. M., 1993. Geographic variations in the thermal and diffusive stability of ground ice on Mars. J. Geophys. Res. 98, 3345–3364.

Mellon, M. T., Jakosky, B. M., 1995. The distribution and behavior of Martian ground ice during past and present epochs. J. Geophys. Res. 100, 11781–11799.

Mellon, M. T., Jakosky, B. M., Postawko, S. E., 1997. The persistence of equatorial ground ice on Mars. J. Geophys. Res. 102, 19357–19370.

Michaels, T. I., Colaprete, A., Rafkin, S. C. R., 2006. Significant vertical water transport by mountain-induced circulations on Mars. Geophys. Res. Lett. 33, 16201.

Montabone, L., Forget, F., Millour, E., Wilson, R. J., Lewis, S. R., Cantor, B., Kass, D., Kleinböhl, A., Lemmon, M. T., Smith, M. D., Wolff, M. J., 2015. Eight-year climatology of dust optical depth on Mars. Icarus 251, 65–95.

Montmessin, F., Forget, F., Rannou, P., Cabane, M., Haberle, R. M., Oct. 2004. Origin and role of water ice clouds in the Martian water cycle as inferred from a general circulation model. J. Geophys. Res. (Planets) 109, E10004.

Moores, J. E., Lemmon, M. T., Rafkin, S. C. R., Francis, R., Pla-Garcia, J., de la Torre Juárez, M., Bean, K., Kass, D., Haberle, R., Newman, C., Mischna, M., Vasavada, A., Rennó, N., Bell, J., Calef, F., Cantor, B., Mcconnochie, T. H., Harri, A.-M., Genzer, M., Wong, M., Smith, M. D., Javier Martín-Torres, F., Zorzano, M.-P., Kemppinen, O., McCullough, E., 2015. Atmospheric movies acquired at the Mars Science Laboratory landing site: Cloud morphology, frequency and significance to the Gale Crater water cycle and Phoenix mission results. Adv. Space Res. 55, 2217–2238.

Pankine, A. A., Tamppari, L. K., Smith, M. D., 2010. MGS TES observations of the water vapor above the seasonal and perennial ice caps during northern spring and summer. Icarus 210, 58–71.

Pla-Garcia, J., Rafkin, S. C. R., Kahre, M., Gomez-Elvira, J., Hamilton, V. E., Navarro, S., Torres, J., Marín, M., Vasavada, A. R., 2016. The meteorology of Gale crater as determined from rover environmental monitoring station observations and numerical modeling. Part I: Comparison of model simulations with observations. Icarus 280, 103–113.

Rafkin, S., Pla-Garcia, J., Kahre, M., Gomez-Elvira, J., Hamilton, H., Marn, M., Navarro, S., Torres, J., Vasavada, A., 2016. The Meteorology of Gale Crater as Determined from Rover Environmental Monitoring Station Observations and Numerical Modeling. Part II: Interpretation. Icarus.

Rivera-Valentin, E. G., Chevrier, V. F., 2015. Revisiting the Phoenix TECP data: Implications for regolith control of near-surface humidity on Mars. Icarus 253, 156–158.

Savijärvi, H., Harri, A.-M., Kemppinen, O., 2016. The diurnal water cycle at Curiosity: Role of exchange with the regolith. Icarus 265, 63–69.

Savijärvi, H. I., Harri, A.-M., Kemppinen, O., 2015. Mars Science Laboratory diurnal moisture observations and column simulations. J. Geophys. Res. (Planets) 120, 1011–1021.

Schofield, J. T., Barnes, J. R., Crisp, D., Haberle, R. M., Larsen, S., Magalhaes, J. A., Murphy, J. R., Seiff, A., Wilson, G., 1997. The Mars Pathfinder Atmospheric Structure Investigation/Meteorology. Science 278, 1752.

Schorghofer, N., Aharonson, O., 2005. Stability and exchange of subsurface ice on Mars. J. Geophys. Res. (Planets) 110.

Skamarock, W. C., Klemp, J. B., 2008. A time-split nonhydrostatic atmospheric model for weather research and forecasting applications. J. Comput. Phys. 227, 3465–3485.

Smith, M. D., 2004. Interannual variability in TES atmospheric observations of Mars during 1999-2003. Icarus 167, 148–165.

Smith, M. D., Wolff, M. J., Clancy, R. T., Murchie, S. L., 2009. Compact Reconnaissance Imaging Spectrometer observations of water vapor and carbon monoxide. J. Geophys. Res. (Planets) 114, 0.

Smith, M. D., Wolff, M. J., Lemmon, M. T., Spanovich, N., Banfield, D., Budney, C. J., Clancy, R. T., Ghosh, A., Landis, G. A., Smith, P., Whitney, B., Christensen, P. R., Squyres, S. W., 2004. First Atmospheric Science Results from the Mars Exploration Rovers Mini-TES. Science 306, 1750–1753.

Smoluchowski, R., 1968. Mars: Retention of Ice. Science 159, 1348–1350.

Spiga, A., Forget, F., 2009. A new model to simulate the Martian mesoscale and microscale atmospheric circulation: Validation and first results. J. Geophys. Res. (Planets) 114, 2009.

Steele, L. J., Balme, M. R., Lewis, S. R., 2017. Regolith-atmosphere exchange of water in Mars' recent past. Icarus 284, 233–248.

Steele, L. J., Lewis, S. R., Patel, M. R., 2014a. The radiative impact of water ice clouds from a reanalysis of Mars Climate Sounder data. Geophys. Res. Lett. 41, 4471–4478.

Steele, L. J., Lewis, S. R., Patel, M. R., Montmessin, F., Forget, F., Smith, M. D., 2014b. The seasonal cycle of water vapour on Mars from assimilation of Thermal Emission Spectrometer data. Icarus 237, 97–115.

Titov, D. V., Markiewicz, W. J., Thomas, N., Keller, H. U., Sablotny, R. M., Tomasko, M. G., Lemmon, M. T., Smith, P. H., 1999. Measurements of the atmospheric water vapor on Mars by the Imager for Mars Pathfinder. J. Geophys. Res. 104, 9019–9026.

Tokano, T., 2003. Spatial inhomogeneity of the martian subsurface water distribution: implication from a global water cycle model. Icarus 164, 50–78.

Tschimmel, M., Ignatiev, N. I., Titov, D. V., Lellouch, E., Fouchet, T., Giuranna, M., Formisano, V., 2008. Investigation of water vapor on Mars with PFS/SW of Mars Express. Icarus 195, 557–575.

Tyler, D., Barnes, J. R., 2015. Convergent crater circulations on Mars: Influence on the surface pressure cycle and the depth of the convective boundary layer. Geophys. Res. Lett. 42, 7343–7350.

Tyler, Jr., D., Barnes, J. R., 2013. Mesoscale Modeling of the Circulation in the Gale Crater Region: An Investigation into the Complex Forcing of Convective Boundary Layer Depths. Mars 8, 58–77.

Wilson, R. J., Neumann, G. A., Smith, M. D., 2007. Diurnal variation and radiative influence of Martian water ice clouds. Geophys. Res. Lett. 34, L02710.

Zent, A. P., Haberle, R. M., Houben, H. C., Jakosky, B. M., 1993. A coupled subsurface-boundary layer model of water on Mars. J. Geophys. Res. 98, 3319–3337.

Zent, A. P., Hecht, M. H., Cobos, D. R., Wood, S. E., Hudson, T. L., Milkovich, S. M., DeFlores, L. P., Mellon, M. T., 2010. Initial results from the thermal and electrical conductivity probe (TECP) on Phoenix. J. Geophys. Res. (Planets) 115, E00E14.

Zent, A. P., Hecht, M. H., Hudson, T. L., Wood, S. E., Chevrier, V. F., 2016. A revised calibration function and results for the Phoenix mission TECP relative humidity sensor. J. Geophys. Res. (Planets) 121, 626–651.

Zent, A. P., Quinn, R. C., 1997. Measurement of H_2O adsorption under Mars-like conditions: Effects of adsorbent heterogeneity. J. Geophys. Res. 102, 9085–9096.

ACCEPTED MANUSCRIPT